International Journal of Pharmaceutics 653 (2024) 123881

Contents lists available at ScienceDirect

International Journal of Pharmaceutics

journal homepage: www.elsevier.com/locate/ijpharm

Cetuximab decorated redox sensitive D-alpha-tocopheryl-polyethyleneglycol-1000-succinate based nanoparticles for cabazitaxel delivery: Formulation, lung targeting and enhanced anti-cancer effects

Aseem Setia [a], Pooja Kumari [b], Vikas [a], Abhishesh Kumar Mehata [a], Ankit Kumar Malik [a], Sanjeev Kumar Mahto [b], Madaswamy S. Muthu [a,*]

[a] Department of Pharmaceutical Engineering and Technology, IIT BHU, Varanasi 221005, UP, India
[b] School of Biomedical Engineering, IIT BHU, Varanasi 221005, UP, India

ARTICLE INFO

Keywords:
Lung cancer
Redox-sensitive
Cetuximab
A549 cell lines
Benzo(a)pyrene
Ultrasound and Photoacoustic Imaging

ABSTRACT

This research work aims to fabricate cetuximab (CTX) decorated cabazitaxel (CBZ) loaded redox-sensitive D-alpha-tocopheryl-polyethyleneglycol-1000-succinate (TPGS-SS) nanoparticles (NPs) for epidermal growth factor receptor (EGFR)-targeted lung tumor therapy. The NPs were prepared using a dialysis bag diffusion method to produce, non-redox sensitive non targeted (TPGS-CBZ-NPs), redox-sensitive nontargeted (TPGS-SS-CBZ-NPs), and targeted redox-sensitive NPs (CTX-TPGS-SS-CBZ-NPs). Developed NPs were characterized for particle sizes, polydispersity, surface charge, surface morphologies, and entrapment efficiency. Moreover, additional *in vitro* studies have been conducted, including *in vitro* drug release, cytotoxicity, and cellular uptake studies. The particle size and charge over the surface were found to be in the range of 145.6 to 308.06 nm and −15 to –23 mV respectively. The IC_{50} values of CBZ clinical injection (Jevtana®), TPGS-CBZ-NPs, TPGS-SS-CBZ-NPs, and CTX-TPGS-SS-NPs were found to be 17.54 ± 3.58, 12.8 ± 2.45, 9.28 ± 1.13 and 4.013 ± 1.05 μg/ml, suggesting the 1.37, 1.89 and 4.37-folds respectively, enhancement of cytotoxicity as compared to CBZ clinical injection, demonstrating a significant augmentation in cytotoxicity. In addition, the *in-vitro* cellular uptake investigation showed that CTX-TPGS-SS-CMN6-NPs accumulated significantly compared to pure CMN6, TPGS-CMN6-NPs, and TPGS-SS-CMN6-NPs in the A549 cells. Furthermore, the targeting efficiency of developed NPs were analysed by ultrasound/photoacoustic and IVIS imaging.

1. Introduction

The fatality rates for both men and women are the highest due to lung cancer, making it the most common cause of cancer related death worldwide. About 238,340 new instances of lung cancer were predicted to be diagnosed in the United States in 2023, according to estimations by the American Cancer Society (Society, 2021). Lung cancer had the highest fatality rate, with 1.80 million deaths out of 2.12 million cases (Sung et al., 2021). Survival rates for lung cancer over the course of five years is 15 %, making it the deadliest form of the disease and a major public health concern around the world. As the second most common disease in both men and women, lung cancer accounts for nearly 2 million annual cases (Alberg et al., 2013; Schluger and Koppaka, 2014; Tao and Imaging, 2019). It is estimated that between 80 and 85 % of lung cancer cases are caused by non-small cell lung cancer (NSCLC) (Łazar-Poniatowska et al., 2021; Zappa and Mousa, 2016). Clinical alternatives for cancer treatment today largely consist of classic techniques like surgery, chemotherapy, and radiation therapy (Housman et al., 2014; Van Meir et al., 2010). There are three main types of NSCLC: adenocarcinoma (40 %), cancer of the squamous cells (25–30 %), and cancer with giant cells (10–15 %) (Mahmood et al., 2017; Meza et al., 2015; Travis, 2012). Almost 70 % of all NSCLCs were already considered to be “advanced” (stages IIIB-IV) upon initial diagnosis because cancer had progressed either locally or to other parts of the body before detection (Lemjabbar-Alaoui et al., 2015). Survival rates at 5 years for stage IIIB NSCLC are around 5 % while stage IV NSCLC (metastatic disease) has a 5-year survival rate of about 1 % (Molina et al., 2008; Wang et al., 2010). In the early stages of NSCLC, surgical removal of the tumor is the best option, but in later stages, systemic treatment is required. Multiple alternatives exist for people with advanced lung

* Corresponding author at: Department of Pharmaceutical Engineering and Technology, IIT BHU, Varanasi 221005, UP, India.
E-mail address: msmuthu.phe@itbhu.ac.in (M.S. Muthu).

https://doi.org/10.1016/j.ijpharm.2024.123881
Received 27 October 2023; Received in revised form 19 January 2024; Accepted 2 February 2024
Available online 5 February 2024

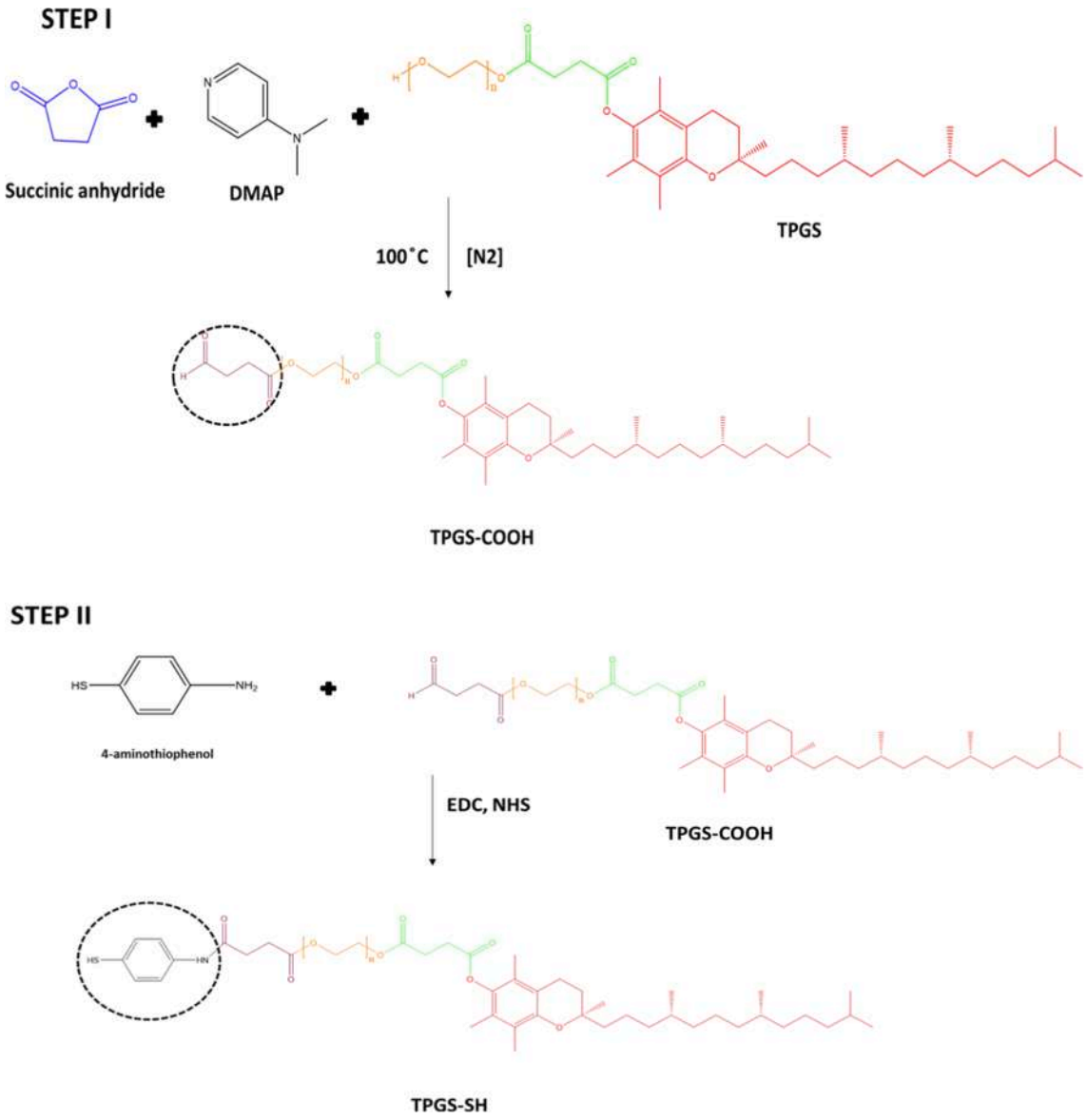

Fig. 1. An illustration depicting the formation of TPGS-SH.

cancer who want to extend their lives and enhance their quality of life (Zhang et al., 2022). Treatments range from surgery and radiation to chemotherapy and targeted immunotherapies, depending on the patient's cancer type, stage, and molecular characteristics of their cancer cells. Stage IIIB NSCLC is typically treated with chemotherapy (Katakami et al., 2012; Stinchcombe et al., 2011).

Cabazitaxel (CBZ) is a microtubule-stabilizing agent that contains anti tumor properties, it is a semisynthetic microtubule stabilizer of the second generation. It is widely used in the treatment of NSCLC, as well as breast and ovarian malignancies (Eskra et al., 2016). Myelosuppression, hypersensitivity, nephrotoxicity, neurotoxicity, and inferior antitumor effectiveness are just some of the dose-dependent side effects associated with the current CBZ clinical formulation (Karavelioglu et al., 2016). Overexpression of particular receptors and an increased redox potential are two hallmarks of cancer cells. These features can be utilized to develop new drug delivery systems with applications in cancer treatment. Cancer cells' higher glycolytic activity and generation of reactive oxygen species (ROS) contribute to this high redox potential (Kumari et al., 2018; Rodic and Vincent, 2018). As a defense mechanism against oxidative stress, an increase in glutathione (GSH) production by cancer cells can decrease sulfhydryl group oxidation and increase protein cleavability (Kennedy et al., 2020). The S-S group of redox sensitive NPs is reduced by GSH after entering to the cancer cells to generate a dithiol intermediate, releasing the medication. Redox-sensitive nanocarrier for improved cancer therapy has recently been developed using 4-amino thiophenol-conjugated with D-alpha-tocopheryl polyethylene glycol 1000 succinate (TPGS) (Yang et al., 2017). TPGS is commonly employed as a penetration enhancer and stabilizing agent. It's an amphiphilic, vitamin E-derived natural product that's been approved by the FDA. In order to better treat NSCLC, extensive research has been conducted on targeted NPs (Jiang et al., 2023). In addition, *in-vivo* imaging in lung cancer applications is made possible by redox-sensitive nanomedicine because of its high levels of potency, selectivity, and responsiveness when loaded with an imaging material (Crucho, 2015). Since the concentration of glutathione in the microenvironment of cancer cells is gradually higher than that found in the circulatory system (2–20 μM), NPs consisting of redox-sensitive disulfide (S-S) bonds are able to release their antineoplastic contents in a target-activated manner. This cleavage of S-S bonds will initiate drug release from nano systems inside cancer cells (Cheng et al., 2011). In light of this, we aimed to investigate the potential benefits of a targeted NSCLC delivery method based on redox-sensitive NPs loaded with CBZ. Since EGFR is overexpressed in NSCLC,

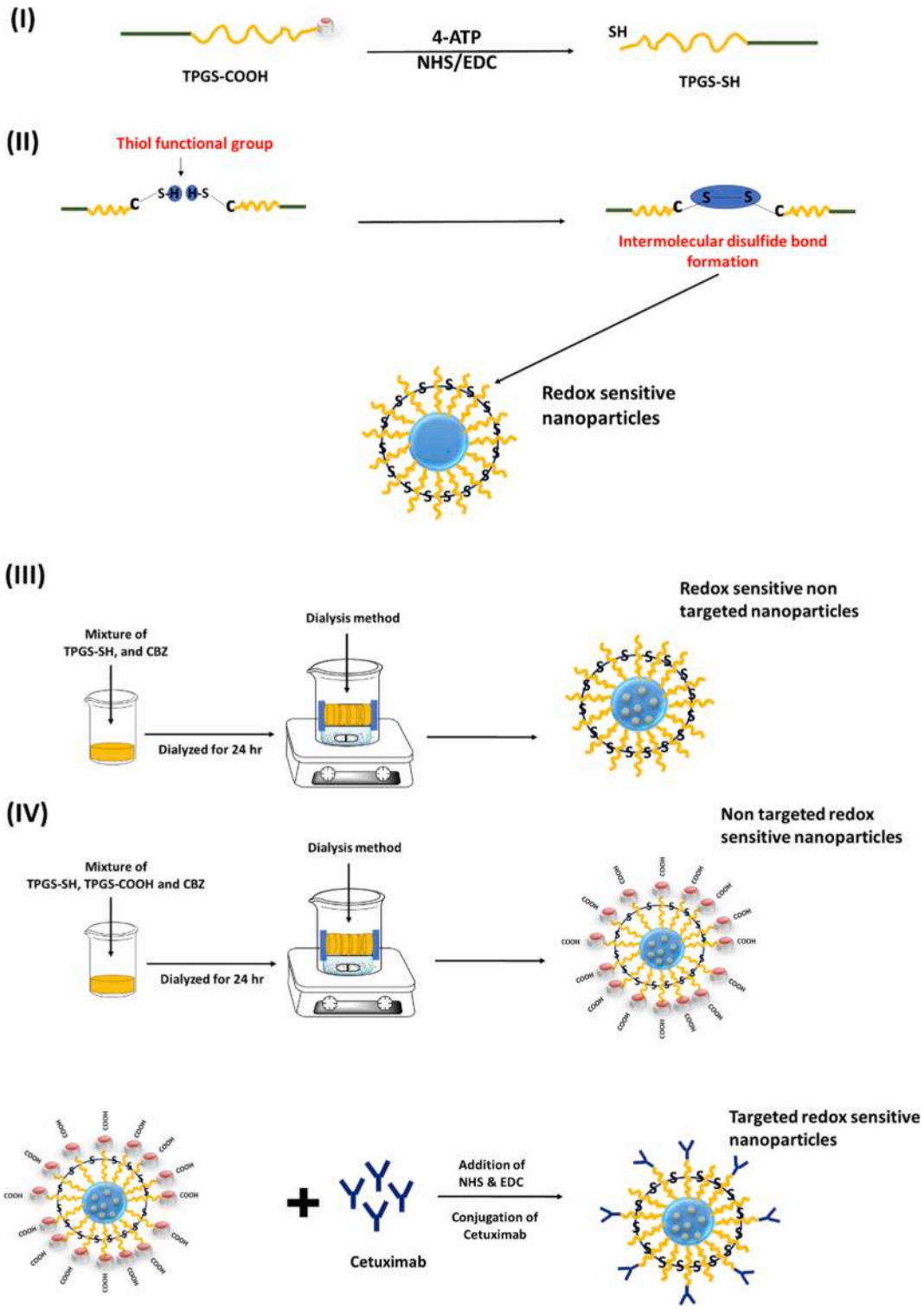

Fig. 2. Schematics of Formulations I) Synthesis of TPGS-SH II) Mechanism of intermolecular disulphide bond formation; III) Redox sensitive non targeted NPs; IV) Targeted-redox-sensitive NPs.

conjugating the epidermal growth factor receptor (EGFR)-specific antibody cetuximab (CTX) over the NPs surface can promote receptor-mediated endocytosis and enable active targeting, facilitating the NPs active delivery into the lung cancer cell (Santos et al., 2021). For this reason, higher GSH levels in the tumor cell may promote the subcellular delivery of the pharmaceutical payload from NPs by facilitating the cleavage of disulfide bonds in a polymer (Sun et al., 2018).

The habit of smoking cigarettes is a major contributor to lung cancer and other types of the disease. Benzo(a)pyrene (B(a)P) is a highly strong carcinogen found in cigarette smoke. DNA adducts are induced by B(a)P reactive metabolites, which can cause mutations (Alexandrov et al., 2010). In a study, John *et al.,* identified two types of DNA adducts after treatment with (B(a)P) which include r7,t8,t9-trihydroxy-c-10-(N ^{2}-deoxyguanosyl)-7,8,9,10-tetrahydrobenzo[a]pyrene (BPdG), and anti-r7,t8-dihydroxy-t-9,10-epoxy-7,8,9,10-tetrahydrobenzo[a]pyrene (BPDE) DNA antiserum which increase the susceptibility of mice for

Table 1
Preparation of NPs via dialysis bag method.

S. No	Formulations	TPGS (mg)	TPGS-COOH (mg)	TPGS-SH (mg)	CBZ (mg)	CMN6 (mg)	CTX (mg)
1	**TPGS-CBZ-NPs**	30	–	–	3	–	–
2	**TPGS-SS-CBZ-NPs**	–	–	30	3	–	–
3	**CTX-TPGS-SS-CBZ-NPs**	–	10	20	3	–	2.5
4	**TPGS- CMN6-NPs**	30	–	–	–	0.3	–
5	**TPGS-SS-CMN6-NPs**	–	–	30	–	0.3	–
6	**CTX-TPGS-SS-CMN6-NPs**	–	10	20	–	0.3	2.5

TPGS-CBZ-NPs: CBZ loaded non-redox sensitive non targeted NPs.
TPGS-SS-CBZ-NPs: CBZ loaded redox sensitive non targeted NPs.
CTX-TPGS-SS-CBZ-NPs: CBZ loaded targeted-redox sensitive NPs.
TPGS-CMN6-NPs: CMN6 loaded non-redox sensitive non targeted NPs.
TPGS-SS-CMN6-NPs: CMN6 loaded-redox sensitive non targeted NPs.
CTX-TPGS-SS-CMN6-NPs: CMN6 loaded targeted-redox sensitive NPs.

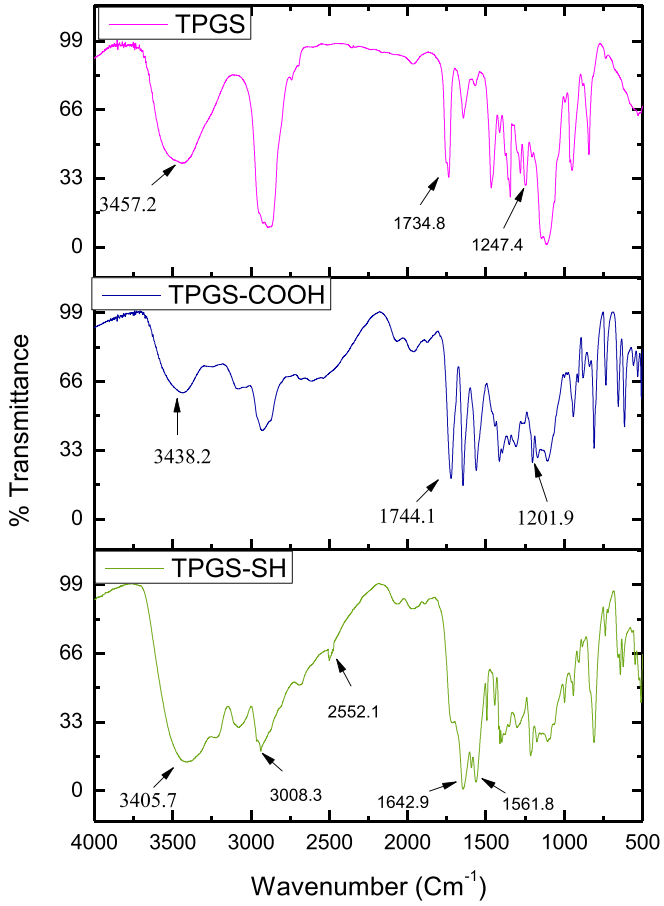

Fig. 3. FTIR spectra of A) TPGS; B) TPGS-COOH; C) TPGS-SH.

lungs cancer development (John et al., 2012). Increased generation of pulmonary inflammatory mediators and activation or facilitation of carcinogenic pathways are both effects of ROS and oxidative stress in the respiratory system (Appel et al., 1990; Chaudhary et al., 2023). In this study, we employed (B(a)P) induced lung carcinoma mice model (Hu et al., 2021) in an effort to prove that redox-sensitive NPs targeting the EGFR could effectively treat lung cancer triggered by cigarette smoke.

Thus, a targeted drug delivery system that enables the targeted

Table 2
FTIR peak assignment of TPGS, TPGS-COOH, and TPGS-SH.

Functional groups	Wave number cm^{-1}		
	TPGS	**TPGS-COOH**	**TPGS-SH**
C = O	1734.8	1744.1	1642.9
O–H	3457.2	3438.2	–
C-O	1247.4	1201.9	–
N–H (stretch)	–	–	3405.7
N–H (bending)	–	–	1561.8
S-H	–	–	2552.1

Table 3
Parameters for the physicochemical analysis of the formulations.

S. No	Formulations	PS (nm)	PDI	ZP (mV)	EE (%)
1	**CBZ control**	–	–	–	–
2	**TPGS-CBZ-NPs**	145.6 ± 11.8	0.342 ± 0.083	−15 ± 1.42	69.3 ± 3.05
3	**TPGS-SS-CBZ-NPs**	221.6 ± 13.5	0.337 ± 0.072	−19 ± 2.14	74.6 ± 2.51
4	**CTX-TPGS-SS CBZ-NPs**	308.06 ± 9.4	0.336 ± 0.059	−23 ± 1.96	79.6 ± 3.05
5	**TPGS- CMN6-NPs**	152.3 ± 14.8	0.364 ± 0.042	−16 ± 2.49	58.7 ± 2.20
6	**TPGS-SS- CMN6-NPs**	226.9 ± 12.2	0.367 ± 0.034	− 21 ± 2.05	67.1 ± 4.63
7	**CTX-TPGS-SS-CMN6-NPs**	316.2 ± 13.8	0.397 ± 0.023	− 26 ± 2.86	71.3 ± 3.56

TPGS-CBZ-NPs: CBZ loaded non-redox sensitive non targeted NPs.
TPGS-SS-CBZ-NPs: CBZ loaded redox sensitive non targeted NPs.
CTX-TPGS-SS-CBZ-NPs: CBZ loaded targeted redox-sensitive NPs.
TPGS-CMN6-NPs: CMN6 loaded non-redox sensitive non targeted NPs.
TPGS-SS-CMN6-NPs: CMN6 loaded redox sensitive non targeted NPs.
CTX-TPGS-SS-CMN6-NPs: CMN6 loaded targeted redox-sensitive NPs.
PS: Particle size; PDI: Polydispersity index; ZP: Zeta potential; EE: Entrapment efficiency.

administration of the loaded medicine to tumours may be a solution for treating lung cancer (Rugamba et al., 2021). Therefore, we have proposed CBZ-loaded EGFR-targeted NPs for the targeted treatment of lung cancer. Firstly, 4-amino thiophenol was conjugated with TPGS (Lian et al., 2017). Secondly, the NPs were prepared by using dialysis bag method and the CBZ was loaded into the non-redox sensitive non targeted NPs (TPGS-CBZ-NPs), and redox sensitive non targeted (TPGS-SS-CBZ-NPs). Third the TPGS-SS-CBZ-NPs were post conjugated with monoclonal antibody to forms targeted redox-sensitive NPs (CTX-TPGS-SS-CBZ-NPs) (Viswanadh et al., 2021). The chimeric monoclonal antibody CTX has a high binding affinity to the EGFR extracellular domain. This is an IgG1 class antibody with both murine and human origins. Its affinity for EGFR is strikingly higher than that for the epithelial growth factor itself. It represents precisely how the CTX can be used to functionalize NPs at much lower concentrations, as a targeted ligand. In addition, NPs whose surfaces have been modified with TPGS have been shown to circulate in the bloodstream for longer time and accumulate in tumors more effectively *in vivo* (Mazzarella et al., 2018). Furthermore, several physicochemical properties were analyzed for the developed NPs, such as particle sizes, polydispersity, zeta potential, surface morphologies, entrapment efficiency, surface chemistry, crystallinity, and *in vitro* performance was studied, evaluating *in-vitro release*, cellular uptake and cytotoxicity (Rani et al., 2023). A549 cell lines were used to analyse the extent of cellular uptake of NPs loaded with coumarin 6 (CMN6). Additionally, IC_{50} values were determined for both nontargeted and targeted NPs in an *in vitro* cytotoxicity assay of CBZ in A549 cells. Additionally, the targeting efficacy of developed NPs were analysed by ultrasound/photoacoustic and IVIS imaging in a B(a)P administered lung carcinoma mice model (Vikas et al., 2023).

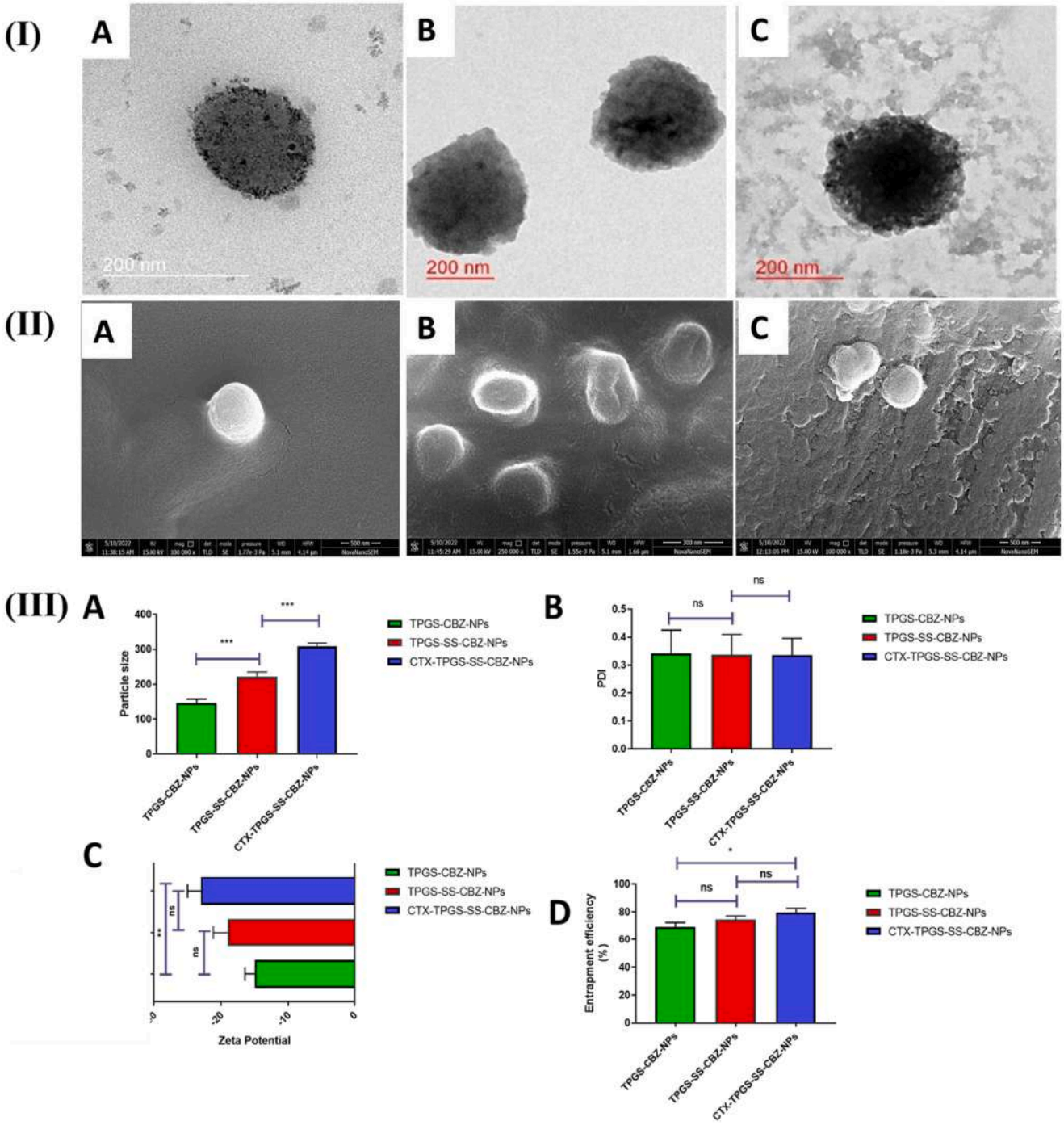

Fig. 4. **(I)** TEM photographs of **A)** TPGS-CBZ-NPs; **B)** TPGS-SS-CBZ-NPs; **C)** CTX-TPGS-SS-CBZ-NPs. **(II)** SEM photographs **A)** TPGS-CBZ-NPs; **B)** TPGS-SS-CBZ-NPs; **C)** CTX-TPGS-SS-CBZ-NPs; **(III)** Statistical comparison of TPGS-CBZ-NPs, TPGS-SS-CBZ-NPs, and CTX-TPGS-SS-CBZ-NPs **A)** Size of the NPs; **B)** PDI; **C)** Surface charge; and **D)** %EE.

2. Materials and method

2.1. Materials

Cabazitaxel gift sample was obtained by Dr. Reddy's Laboratories in Hyderabad, India. The following chemicals such as 1-Ethyl-3-(3-dimethylaminopropyl) carbodiimide (EDC), DMAP (4-dimethylaminopyridine), benzopyrene, 4-aminothiophenol (4 ATP), Cetuximab, N-hydroxy succinimide (NHS), methylene blue (MB) and coumarin-6 (CMN6) were procured from Sigma-Aldrich, USA. The TPGS (D-alpha-tocopheryl-polyethyleneglycol-1000-succinate) was provided as a gift sample by Antares Health Products. The 1 kDa dialysis membrane was purchased from Sigma-Aldrich®, Spectrum Labs-Bioz, USA. Cell lines A549 were obtained from NCCS, Pune, India. Biotium, USA, provided the MTT. The following materials were supplied by HIMEDIA laboratories: fetal bovine serum, Dulbecco's modified Eagle's medium (DMEM), paraformaldehyde solution (4 %), 4′,6-diamidino-2-phenylindole (DAPI), propidium iodide (PI), and antibiotics solution 100X liquid. 1,1′-Dioctadecyl-3,3,3′,3′-tetramethylindodicarbocyanine,4-chlorobenzenesulfonate salt (DiD dye) was procured by Thermo Fisher Scientific, India. In addition to the chemicals and reagents used in the analysis, all other materials used were analytical grade.

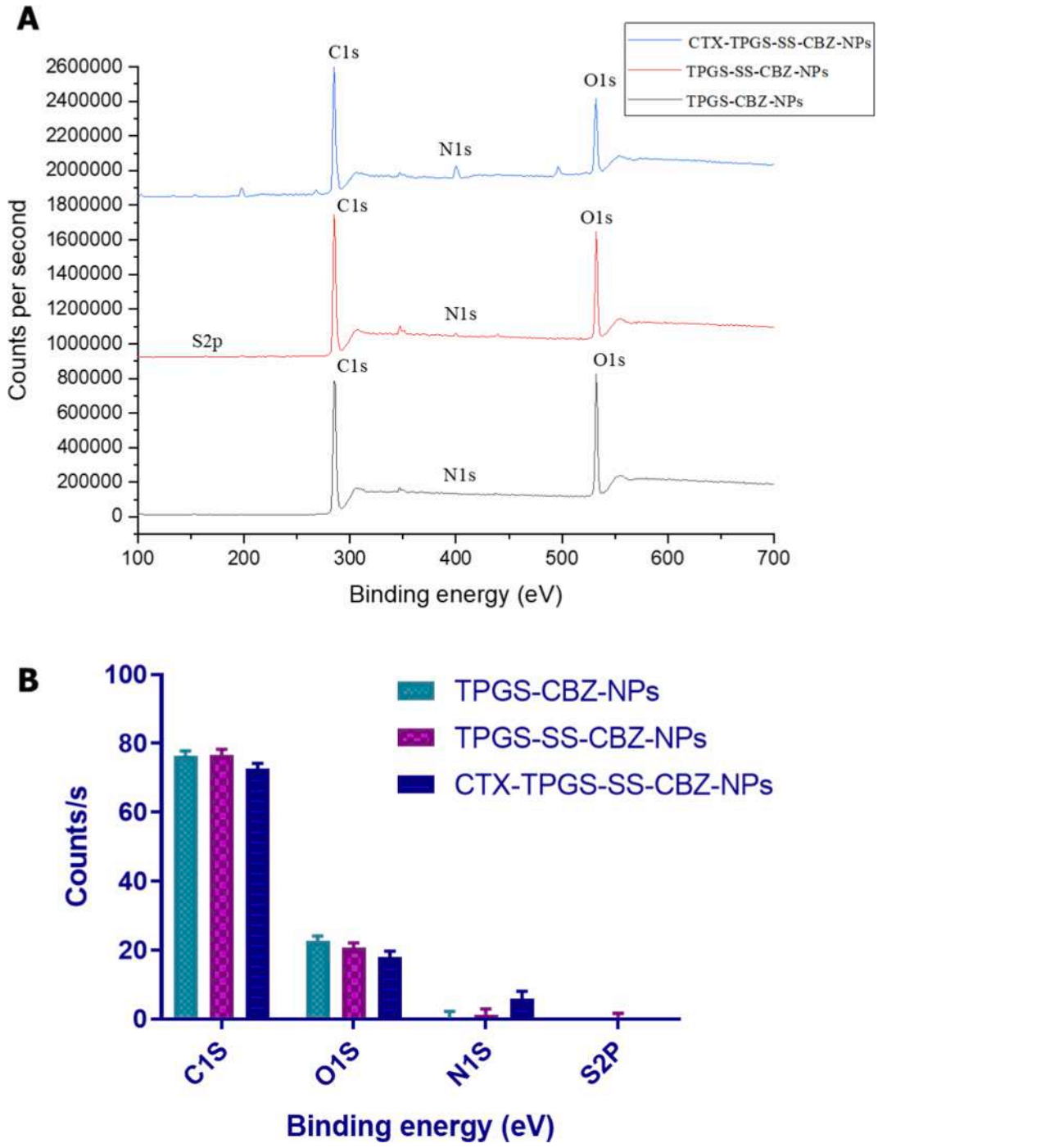

Fig. 5. A) XPS survey of **i)** TPGS-CBZ-NPs **ii)** TPGS-SS-CBZ-NPs; and **iii)** CTX-TPGS-SS-CBZ-NPs and **B)** In an XPS survey, the atomic percentage of atoms was shown in a histogram **i)** TPGS-CBZ-NPs **ii)** TPGS-SS-CBZ-NPs; and **iii)** CTX-TPGS-SS-CBZ-NPs.

2.2. Methods

2.2.1. Synthesis of conjugates and preparation of self-assembled micelles

2.2.1.1. Synthesis of TPGS-SH. As shown in Fig.1, TPGS-SH was synthesised in two stages. In the first stage, TPGS is functionalized with a free carboxyl group at its terminal by subjecting succinic anhydride and DMAP to a ring-opening reaction in a nitrogen environment at 100 °C for 24 h. In accordance with previous reports, all reaction conditions were maintained (Muthu et al., 2015). The TPGS-SH conjugate was made by combining the carboxylate groups of TPGS with 4-ATP using EDC and NHS to make amine-reactive esters. The EDC and NHS were combined with the TPGS-COOH at a molar ratio of 1:2. After 3 h of gentle stirring at 25 °C and pH 5, an addition of a 1:1 ethyl alcohol solution of 4-ATP (10 mL) was made to the mixture. The reaction was left to stand in the dark at 4 °C overnight. Sodium borohydride was used to neutralize acidity without disrupting the disulfide bonds, bringing the pH back to 7. The thiol groups in this procedure were protected from oxidation by nitrogen. Ethyl alcohol was used for the precipitation of the reaction mixture. When the purification process was complete, the solution was lyophilized by being frozen. Finally, TPGS-SH was formsed as a pale-yellow product (Viswanadh et al., 2021). The prepared thiolated TPGS exists in reduced form, but when two molecules of thiolated TPGS comes closer then it forms an intermolecular disulfide bond (S-S) as oxidized form **(**Fig. 2**II)** (Alberts, 2017).

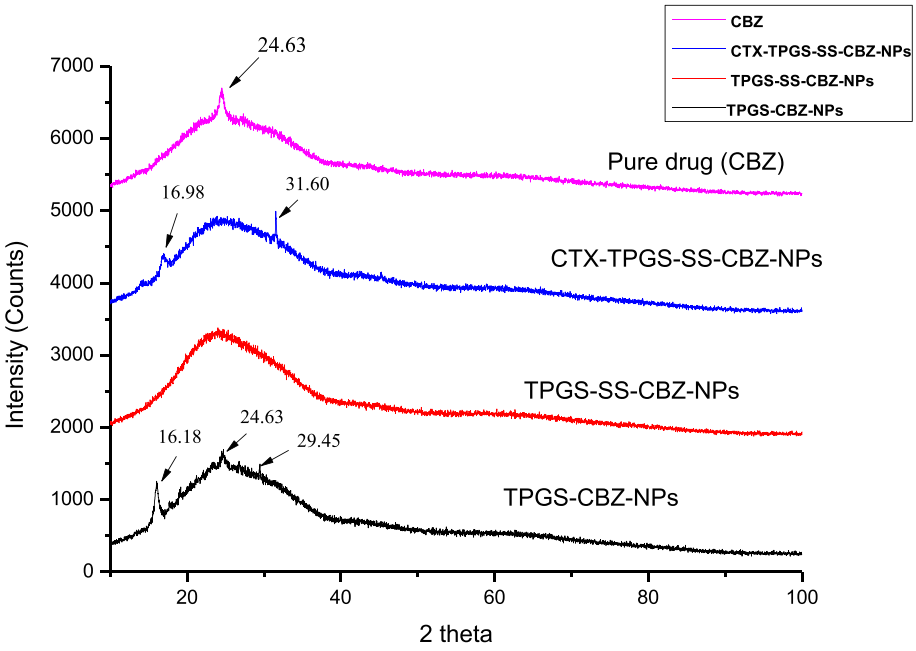

Fig. 6. XRD pattern of CBZ, CTX-TPGS-SS-CBZ-NPs, TPGS-SS-CBZ-NPs, and TPGS-CBZ-NPs.

2.2.1.2. Analysis of TPGS conjugates. The prepared TPGS conjugates were characterized by FTIR and ^{1}HNMR spectroscopy. The FTIR (Nicolet™ iS™ 5 spectrometer, Thermo Fisher Scientific, USA) spectroscopy was used to characterize the prepared TPGS integrates. The analysis relied on an FTIR spectrometer. Using the potassium bromide pellet method, FTIR spectra of the samples was acquired by scanning across a range of 4000 to 600 cm^{-1} (Jithan et al., 2011). The ^{1}H NMR spectra of TPGS conjugates were recorded at 500 MHz using a BRUKER BioSpin International NMR spectrometer (Gill et al., 2012). The amount of 4-ATP conjugated with TPGS carboxylate was determined spectrophotometrically using Ellman's reagent at λmax of 240 nm (Sun et al., 2018). The ethanol was used to prepared the 4-ATP calibration curve at a concentration of 20–120 μg/mL. Further, in a 96 well plates 80 μL of the prepared stock solution was placed with Ellman's reagent (160 μL). Then, 8 mg of TPGS-SH was solubilized in 10 mL of ethanol, and 80 μL of the solution was placed with Ellman's reagent (160 μL). The 4-ATP calibration curve was used to quantify the percent quantity of 4-ATP conjugated with TPGS carboxylate.

2.2.1.3. Preparation of self-assembled micelles of cabazitaxel/methylene blue (MB)/coumarin-6 (CMN6)/DiD dye. The TPGS-CBZ-NPs, and TPGS-SS-CBZ-NPs were synthesized using the dialysis technique as illustrated in Table 1, and the schematic is shown in Fig. 2**.** The TPGS-CBZ-NPs were prepared by dissolving CBZ in a mixture of TPGS-DMSO. After that, the solution was dialyzed for 24 h against milli-Q water. After the allotted amount of time had passed, the newly generated NPs were centrifuged out of the mixture at 16,802 xg, milli-Q water was used for three separate washings before being reconstituted in the water. Moreover, the same process was repeated for TPGS-SS-CBZ-NPs. However, the CTX-TPGS-SS-CBZ-NPs were prepared in a manner similar to that described above, except that NPs were made using a combination of TPGS-SS and TPGS-COOH (at a ratio of 20:10). The EDC/NHS (1:5) was used to surface-conjugate with cetuximab, which activates carboxylate groups on the NPs. After that, we added 2.5 mg of cetuximab to the NPs suspension and mixed it for another 30 min. To eliminate the free drugs and reactants, the resultant formulation was dialyzed against a saturated solution of CBZ via a membrane of 1 kDa (Viswanadh et al., 2021).

For the cellular-uptake study, a batch of CMN6-loaded TPGS-CMN6-NPs, TPGS-SS-CMN6-NPs, and CTX-TPGS-SS-NPs were developed. For photoacoustic imaging, we additionally synthesized a series of MB-loaded TPGS-MB-NPs, TPGS-SS-MB-NPs, and CTX-TPGS-SS-MB-NPs using 50 μg of MB dye in place of CBZ. Finally, DiD-loaded TPGS-DiD-NPs, TPGS-SS-DiD-NPs, and CTX-TPGS-SS-DiD-NPs were prepared using the same method, except 2 μg of DiD dye was employed in place of CBZ for IVIS fluorescence imaging.

2.2.2. Evaluation of prepared micelles for their physicochemical characteristics

2.2.2.1. Measurement of the size of particles, polydispersity, and surface charge. The size of the NPs, polydispersity index, and surface characteristics of the NPs were all measured at 25 °C using DLS (Malvern Zeta sizer Nano series) (Pooja et al., 2014). All the study was performed in triplicate (n = 3).

2.2.2.2. Transmission electron microscopy studies. The finished NPs were analysed by TEM (Philips CM-12, Fullerton, CA) to determine their internal structure and exterior shape. Every nanoparticle formulation was sonicated for two minutes after being diluted five times with milli-Q water. After placing a single drop of each diluted sample on TEM grids and drying them overnight in a vacuum, and TEM was used to examine the samples (Antoniou et al., 2015).

2.2.2.3. Scanning electron microscopy studies. After the NPs had been formed, their surface characteristics was analysed using a scanning electron microscope (MA15/18, CARL ZEISS MICROSCOPY LTD). At 20 kV and 50 KX magnification, images were taken. Before being deposited on coverslips, each sample was diluted up to five times in ultra-pure water and dried at 40 °C for 24 h in a hot air oven. The relevant slides were coated with carbon before the SEM study (Agarwal et al., 2018).

2.2.2.4. X-ray diffraction analysis. The XRD analysis on pure drug (CBZ), TPGS-CBZ-NPs, TPGS-SS-CBZ-NPs, and CTX-TPGS-SS-CBZ-NPs was done using Bench Top X-Ray Diffraction (BT-XRD: RIGAKU Corporation). The excipients, medications, and their final products are characterised by their crystalline peaks using a technique called X-ray diffraction (XRD). The crystal structure of the drugs in the formulation was determined. The samples were subjected to a voltage of 40 kV and a current of 15 mA, the scanning range of the samples was (2θ), and the

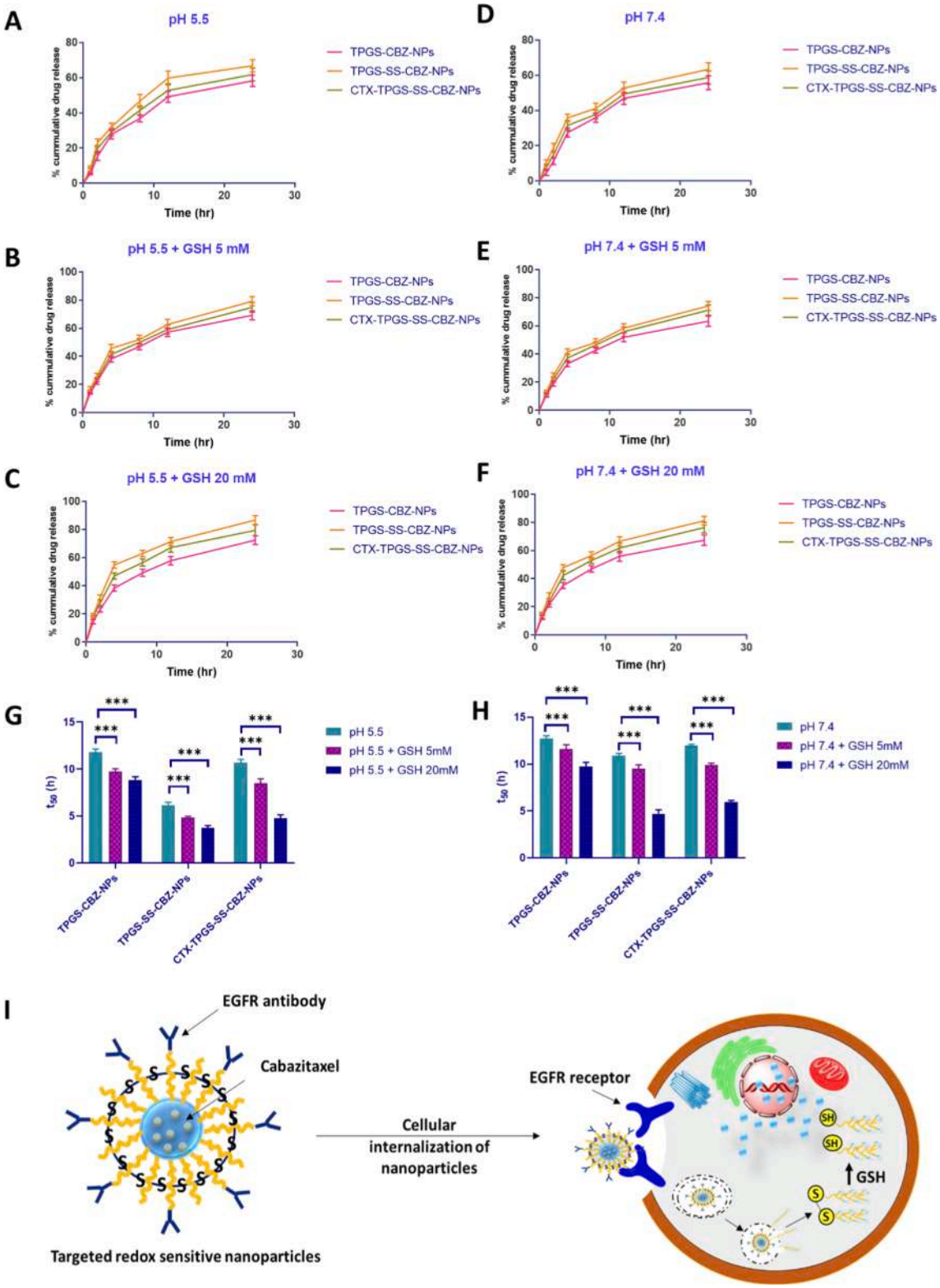

Fig. 7. *In vitro* drug release profile **A)** pH 5.5**B)** pH 5.5 with GSH 5 mM; **C)** pH 5.5 with GSH 20 mM; **D)** pH 7.4 **E)** pH 7.4 with GSH 5 mM; **F)** pH 7.4 with GSH 20 mM; **G & H)** t_{50} values of NPs at various pH range; **I)** Mechanism of cellular internalization of targeted redox sensitive nanoparticles.

scan speed was 7°/min (Shen et al., 2020).

2.2.2.5. Surface chemistry. An X-ray photoelectron spectroscopy analysis (K-Alpha, Thermo Fisher Scientific) was performed to study the surface chemistry of NPs. Exploration of binding energies between 100 and 800 electron volts (eV) was performed. The samples were prepared by dropping NPs suspension on a glass slide (1x1 cm) and drying them under a vacuum overnight. The surface chemistry of prepared TPGS-CBZ-NPs, TPGS-SS-CBZ-NPs, and CTX-TPGS-SS-CBZ-NPs was studied by XPS (Jha et al., 2020).

2.2.2.6. Entrapment efficiency and drug loading capacity. Encapsulation

Table 4
The t_{50} values of various formulations at pH 5.5 + GSH 5 mM, pH 5.5 + GSH 20 mM, pH 7.4 + GSH 5 mM, and pH 7.4 + GSH 20 mM.

Formulations	pH 5.5 (hr)		pH 5.5 + GSH 5 mM (hr)		pH 5.5 + GSH 20 mM (hr)		pH 7.4 (hr)		pH 7.4 + GSH 5 mM (hr)		pH 7.4 + GSH 20 mM (hr)	
	Mean	SD	Mean	SD	Mean	SD	Mean	SD	Mean	SD	Mean	SD
TPGS-CBZ-NPs	11.42	0.14	9.48	0.13	8.47	0.21	12.36	0.14	11.17	0.14	9.34	0.15
TPGS-SS-CBZ-NPs	5.87	0.12	4.70	0.12	3.47	0.14	10.69	0.21	9.05	0.25	4.34	0.23
CTX-TPGS-SS- CBZ-NPs	10.36	0.14	8.04	0.13	4.46	0.16	11.75	0.36	9.71	0.36	5.73	0.34

efficiency of the produced NPs was evaluated using HPLC (LC-20AR, Shimadzu, Japan). Our experiment involved an evaporator-rotary drying of 200 μL of NPs equivalent to 60 μg of CBZ. After the solvent was taken out, the NPs that were left were treated with methanol and stirred in a vortex for 12 h. Nearly, 10 min of centrifugation at 5813 xg separated the solution, then a rotary evaporator was used to dehydrate the supernatant. The experiment used a mobile phase consisting of 75 % methanol and 25 % water. CBZ was reconstituted in 1 mL of mobile phase by being vortexed for 10 min. Before being added to the HPLC vials, a 0.22 μm membrane filter was used to filter the specimens (Kommineni et al., 2019). Mobile phase CBZ standard concentrations were used to generate a standard curve, which was then plotted against the peak area. The entrapment efficiency was determined using the following formula:

$$\text{Entrapment efficiency}\,(\%) = \frac{\text{Drug entrapped in the NPs}}{\text{Drug added in the NPs preparation process}} \text{x}\,100$$

The % drug loading of the NPs was calculated by using following formula:

$$\textit{Drug loading}(\%) = \frac{\text{Amount of drug}}{\text{weight of lyophilized NPs}} \text{x}\,100$$

2.2.2.7. Detection of CTX concentrations. The CTX-TPGS-SS-CBZ-NPs were prepared and CTX concentration was determined by Bradford assay. The CTX-TPGS-SS-CBZ-NPs, a blank PBS solution with a pH of 7.4, and standard CTX solution were each produced at 1 mL and given 5 min to react with 5 mL Bradford reagent before their UV absorbances were measured. After that, we employed a bovine serum albumin (BSA) calibration curve to figure out how much CTX had been conjugated onto the specific redox-sensitive NPs (Kutty and Feng, 2013). A conjugation degree can be assessed using the following equation:

$$\textbf{Extent of conjugation of CTX} = \frac{\textit{Amount of CTX in targeted redoxsensitive NPs} - \textit{CTX amount in blank (PBS)}}{\textit{amount detected in standard CTX solution}} X100$$

2.2.3. In vitro studies

2.2.3.1. In-vitro drug release. To simulate the physiological reductive condition, two distinct buffers (pH 5.5 and 7.4) with GSH amounts of (5 and 20 mM) were used to examine the *in vitro* release pattern of CBZ from NPs. Dialysis clips were used to close a dialysis bag made of cellulose membrane (1 kD) containing a drug-loaded NPs suspension in a buffer containing glutathione (GSH). The bag was then immersed in a beaker containing media made up of the same buffer (50 mL) at 37 ± 0.5 °C with constant stirring at 100 rpm. Following the withdrawal of 2 mL samples at regular intervals, the same amount of fresh media was replaced. For quantification of the released drug concentration, HPLC was used (Xue et al., 2016). *In vitro* drug release data were analysed for drug release kinetics by applying the zero order, first order, higuchi order and peppas exponential models (Muthu and Singh, 2009).

2.2.3.2. In-vitro cytotoxicity study. The MTT assay was used to test the cytotoxicity of the CBZ control, TPGS-CBZ-NPs, TPGS-SS-CBZ-NPs, CTX-TPGS-SS-CBZ-NPs on lung cancer A549 cells. This was accomplished by seeding at a density of 1 x 10^3 cells per well into 96 well plates and incubating them for 24 h to promote proper cell adhesion. Subsequently, the cells were subjected to varying levels of CBZ in DMEM (0.025, 0.25, 2.5, and 25 μg/ml) for 24 h, along with TPGS-CBZ-NPs, TPGS-SS-CBZ-NPs, and CTX-TPGS-SS-CBZ-NPs at equivalent concentration. The cells were washed with PBS in order to remove adhere drug and formulations. Briefly, fresh DMEM with 10% MTT (5 mg/mL) was added in each well, and incubated for 4h. Further MTT solution was discarded and 100 μL of DMSO solution was used to dissolve the formazan crystals. After that, the optical density at 570 nm was observed using the microplate reader. The treated cells were tested for cytotoxicity in comparison to their untreated counterparts. After incubation with cells for 24 h at 37 °C, the cytotoxicity produced by TPGS-CBZ-NPs, TPGS-SS-CBZ-NPs, and CTX-TPGS-SS-CBZ-NPs in accordance to CBZ control was assessed in the A549 cells (Cafaggi et al., 2007). According to the following formula, the proportion of living cells was calculated:

$$\%\ \textbf{\textit{Cellular viability}} = \frac{\textit{Absorbance of the treated cells}}{\textit{Absorbance of the control cells}} X100$$

2.2.3.3. In vitro cellular uptake study. An assessment of the extent to which CMN6-loaded NPs are taken up by cells (TPGS-CMN6-NPs, TPGS-SS-CMN6-NPs, and CTX-TPGS-SS-CMN6-NPs) was evaluated on A549 cells by using confocal laser scanning microscopy (CLSM). To determine whether the A549 cells were taken up, they were seeded at 50,000 per well in a six-well plate. After incubating the plates for at least 24 h, 5 μg/ml of pure CMN6, TPGS-CMN6-NPs, TPGS-SS-CMN6-NPs, and CTX-TPGS-SS-CMN6-NPs were added to each wells. One well was pre-treated with CTX before incubation with CTX-TPGS-SS-CMN6-NPs to assure the unambiguous role of EGFR in the intracellular uptake of NPs. A multi-step washing procedure, followed by a fixation by 4% para-formaldehyde, was conducted after the cells had been exposed for 2 h. The cells were washed twice with cold PBS followed by 0.1 %Triton X-100 for permeabilization. Propidium iodide (10 μg/mL) was incubated with the cells for an additional 40 min to stain the nuclei. CLSM was used to observe the monolayer of cells after three washes with PBS (Muthu et al., 2012).

2.2.3.4. Apoptosis study with DAPI/PI dual staining. The DAPI/PI dual-stating approach was used to test the apoptotic potential of both the free drug and the NPs. Briefly, 1 x 10^5 A549 cells were added in each well of 12 well cell culture plate. The cells were then exposed with free CBZ, TPGS-CBZ-NPs, TPGS-SS-CBZ-NPs, CTX-TPGS-SS-CBZ-NPs for 24 h

in a CO_2 incubator. Furthermore, the cells were washed with PBS and stained for 30 min using DAPI (1 μg/mL)/PI (10 μg/mL). After that, the cells were visualized using CLSM microscope (Morales-Cruz et al., 2016).

2.2.4. *In-vivo studies*

2.2.4.1. Ethical approval. The *in vivo* animal experimental studies were approved by the Institutional Animal Ethics Committee (IAEC), Faculty of Medicine, Institute of Medical Science (BHU) Varanasi (IAEC Approval Number: Dean/2019/IAEC/1226). Each animal experiment followed strict guidelines published by the National Research Council.

2.2.4.2. Carcinogen induced lung cancer model. Swiss albino mice weighing between 15 and 20 g were used in the experiment. Housing for the animals included climate and humidity regulation. To induce cancer, B(a)P was administered orally at a dose of 50 mg/kg in corn oil. It took four weeks of twice-weekly B(a)P injections to cause lung cancer. On the other hand, an extra set of cancer model subjects was examined on the 14th day to observe the onset of cancer induction.

2.2.4.3. Ultrasound and photoacoustic imaging for monitoring the lung distribution of nanomedicine in mice. Methylene blue (MB) loaded NPs were evaluated *in vivo* using a multimodal imaging system in a B(a)P administered lung carcinoma. In this experiment, male Swiss albino mice were utilised (n = 3), and their body weight ranged from 16 to 20 g. These mice were fed with a regular mice diet and housed in a controlled setting with regular access to water. The NPs were administered through the lateral tail vein in mice at a dose of 1.5 mg/kg. Injections of MB control, TPGS-MB-NPs, TPGS-SS-MB-NPs, and CTX-TPGS-SS-MB-NPs were given to five groups of mice, separately. In addition to the cancer model, CTX-TPGS-SS-MB-NPs were administered into cancer free mice to evaluate biodistribution. During the experiment, the mice were sedated with inhalational isoflurane (Induction: 3 %; Maintenance: 1.5 %-2%).

The animals were then laid supine on a warm operating table (Fujifilm Visual Sonics, Inc.). Superior parasternal long-axis lung imaging was achieved by positioning transducer encased in a jacket holding a compact (14 mm) optical fibre bundle (Fujifilm Visual Sonics, Inc.) placed over the body of mice. Ultrasonic gel (BPL, India) without bubbles was utilize to develop the gap of 5 mm between the skin of animal and transducer. Throughout all scans, the depth of the pictures was 18 mm. An intravenous injection of NPs loaded with MB was administered in 30-minute intervals before and after MB control. Prior to injecting NPs, an initial photoacoustic signal baseline value was used to split all scans. Prior to injecting the NPs, every scan was subtracted from a baseline PA signal of haemoglobin to reduce the PA signal (Xu et al., 2022).

2.2.4.4. Live imaging of the lungs with IVIS. Images of free DiD and DiD-loaded NPs were captured from B(a)P administered carcinoma animals with the Photon Imager Optima System (Biospace Lab). Fluorescence signals were collected at 620 nm for excitation and 710 nm for emission at various times following the injection of NPs (which equates to 200 nM associated with DiD dye), varying from 10 min, 2 h, 4 h, 6 h, and 24 h. We evaluated the lung region for its luminous efficiency using the ROI tool in the imaging software from Biospace Lab (defined here as fluorescence intensity per unit area per unit time) (Cao et al., 2015).

2.2.4.5. Histopathology study. To compare the produced NPs to the CBZ control for safety, a histopathology examination was conducted on Wistar rats. In this study, five groups of rats, with five rats in each were used as experimental subjects. The saline group served as the placebo, while the other four groups got either CBZ control, TPGS-CBZ-NPs, TPGS-SS-CBZ-NPs, or CTX-TPGS-SS-CBZ-NPs with a dosage of 6.5 mg/kg. Two weeks after receiving the formulations three times intravenously every three days, the rats were sacrificed. Haematoxylin and eosin (H&E) staining of sections of the lungs, liver, kidneys, heart, and brain were performed. Light microscopy (Olympus, India) was employed to detect the alterations in histopathology, and Top View 3.7 was used to obtain images (Nomier et al., 2022).

2.2.4.6. Assessing the anticancer effectiveness of nanoparticles in mice. The Swiss albino mice were divided into six groups comprising of six animals in each group (n = 6). Group I animals were considered as a negative control, and received four weeks of oral corn oil. Group II animals, who served as positive controls, were given B(a)P, at a dose of 50 mg/kg body weight orally solubilise in corn oil twice weekly for four weeks to develop the lung carcinoma and dosing was continued to 120 days. The treatments were administered intravenously twice weekly via the tail vein of mice at a dose of 6.5 mg/kg of CBZ following the fourteenth day of being exposed to B(a)P and the treatment were continued up to four weeks. In Group III, the animals were given a four weeks course of CBZ control. Animals in Groups IV, V, and VI were administered TPGS-CBZ-NPs, TPGS-SS-CBZ-NPs, and CTX-TPGS-SS-CBZ-NPs (6.5 mg/kg body weight of CBZ, intravenously) for four weeks. Histopathological findings validated the induction of lung cancer in positive control group. All animals had their lungs removed on the day of death; those that did not undergo this procedure were euthanized after 120 days so that histological investigation could be conducted. Following that, the lungs were extracted and preserved with 10 % formalin, and paraffin was used for blocking. Next, distinct glass slides were used to

Table 5
In Vitro Drug Release Kinetics of TPGS-CBZ-NPs, TPGS-SS-CBZ-NPs, and CTX-TPGS-SS-CBZ-NPs.

Batches	Drug release kinetics, Correlation coefficients (r^2)			Release Exponent (n)
	Zero order	First order	Higuchi order	
pH 5.5				
TPGS-CBZ-NPs	0.8381	0.9097	0.9647	0.513
TPGS-SS-CBZ-NPs	0.7978	0.8877	0.9547	0.461
CTX-TPGS-SS-CBZ-NPs	0.8211	0.9038	0.9641	0.481
pH 5.5 + 5 mM				
TPGS-CBZ-NPs	0.8064	0.9184	0.9697	0.427
TPGS-SS-CBZ-NPs	0.8077	0.9505	0.9691	0.415
CTX-TPGS-SS-CBZ-NPs	0.8175	0.9446	0.9738	0.430
pH 5.5 + 20 mM				
TPGS-CBZ-NPs	0.8215	0.9404	0.9778	0.432
TPGS-SS-CBZ-NPs	0.7509	0.9451	0.9433	0.380
CTX-TPGS-SS-CBZ-NPs	0.7736	0.9264	0.9571	0.396
pH 7.4				
TPGS-CBZ-NPs	0.8321	0.8998	0.9544	0.531
TPGS-SS-CBZ-NPs	0.8089	0.9035	0.9634	0.445
CTX-TPGS-SS-CBZ-NPs	0.8204	0.8984	0.9607	0.482
pH 7.4 + 5 mM				
TPGS-CBZ-NPs	0.8211	0.9142	0.9729	0.452
TPGS-SS-CBZ-NPs	0.8148	0.9414	0.9696	0.433
CTX-TPGS-SS-CBZ-NPs	0.8332	0.9448	0.9776	0.455
pH 7.4 + 20 mM				
TPGS-CBZ-NPs	0.8101	0.9146	0.8101	0.435
TPGS-SS-CBZ-NPs	0.7831	0.9413	0.9717	0.412
CTX-TPGS-SS-CBZ-NPs	0.8044	0.9378	0.9666	0.434

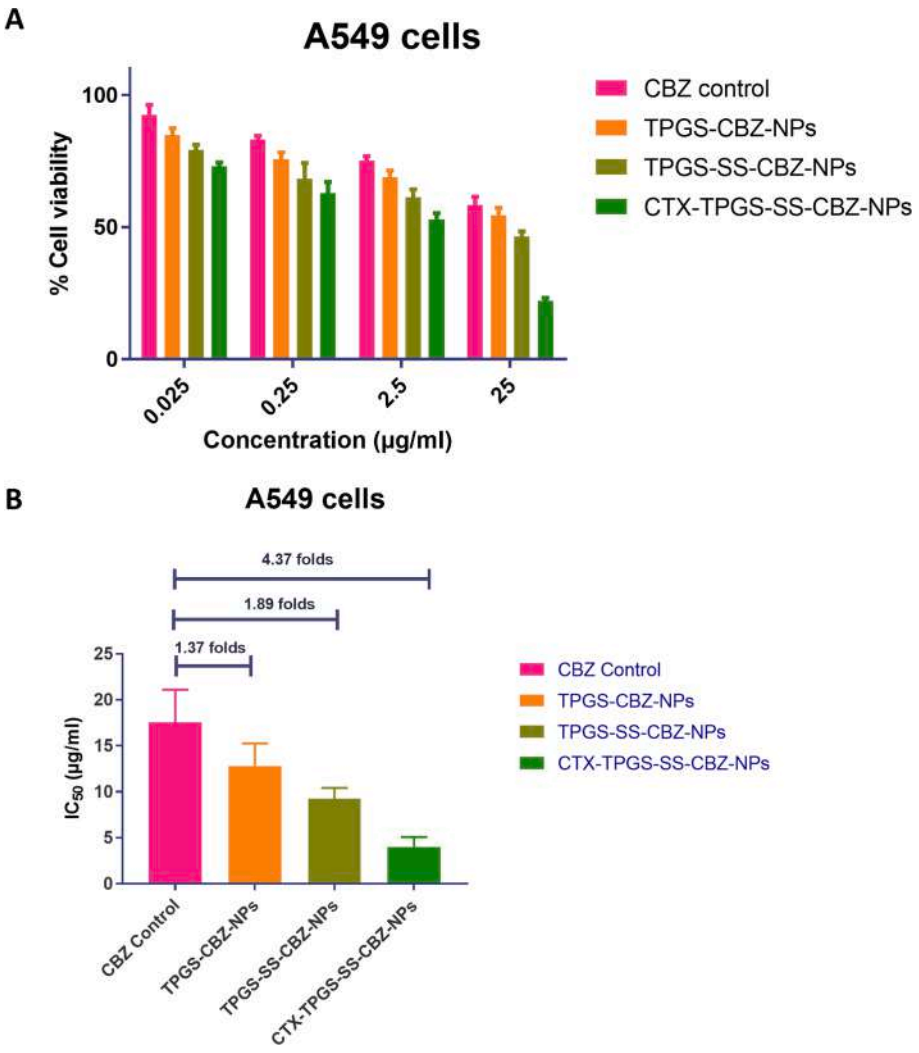

Fig. 8. A) Cellular cytotoxicity assessment of the CBZ control, TPGS-CBZ-NPs, TPGS-SS-CBZ-NPs, CTX-TPGS-SS-CBZ-NPs; and **B)** Graph depicting the IC_{50} values in A549 cells.

mount paraffin slices with a thickness of 5 µm following standard processing. After H&E treatment, the aforementioned slices were examined for cancer cell counts using ImageJ software (Vikas et al., 2023).

2.2.4.7. Statistical evaluation. *In vitro* and *in vivo* results were presented as means and standard deviations for the purposes of statistical analysis. The statistical analysis was performed in GraphPad Prism 7.0. To determine statistical significance between groups, we employed a one-way analysis of variance and *t*-test. There were four levels of statistical significance: ns ($p > 0.05$), * ($p < 0.05$), ** ($p < 0.01$), *** ($p < 0.001$).

3. Results and discussion

3.1. Characterization of TPGS conjugates

To compare the infrared spectra of TPGS, TPGS-COOH, and TPGS-SH, the FTIR investigation was conducted (Fig. 3. **and** Table. 2). In TPGS, the existence of a wide O–H signal at 3457.2 cm^{-1} is indicative of a free hydroxyl group. Additionally, the ester C = O stretching vibration was detected at 1734.8 cm^{-1}. However, the C = O stretching vibration of the ester has been seen to be stronger at 1744.1 cm^{-1} in TPGS-COOH. The TPGS-COOH contains a carboxylic acid terminal group exhibiting O–H stretching at 3438.2 cm^{-1}. At 3405.7 cm^{-1}, the TPGS-SH shows a peak in N–H stretching, and at 1561.8 cm^{-1}, the TPGS-SH displays a peak in N–H bending. However, a carbonyl group of the amide linkage was found at 1642.9 cm^{-1}. Moreover, the detection of an SH peak at 2552.01 cm^{-1} suggests the development of thiolated TPGS. The ^{1}HNMR spectra of TPGS-COOH, and TPGS-SH have been presented in our previous publication (Viswanadh et al., 2021). It has been observed that the methylene group of the conjugated succinic group contributes to the peaks at 2.38 and 3.00 ppm that have been observed in TPGS-COOH spectra. The 4-ATP's thiol group is shown by the peak in its spectral line at 3.44 ppm. Moreover, the peaks for aromatic protons were observed at 6 to 7 ppm, which was absent in the spectra of TPGS-COOH. The 4-ATP's thiol group is shown by the peak in its spectral line at 3.44 ppm. Moreover, the peaks for aromatic protons were observed at 6 to 7 ppm, which was absent in the spectra of TPGS and TPGS-COOH. The amount of 4-ATP that has been conjugated with TPGS- COOH was determined spectrophotometrically using Ellman's reagent. The amount of 4-ATP conjugated with TPGS-COOH was found to be 58.7 ± 8.4 %.

3.2. Physicochemical analysis

3.2.1. Assessment of particle size, PDI and charge over the surface of NPs

In the study of prepared TPGS-CBZ-NPs, TPGS-SS-CBZ-NPs, and CTX-TPGS-SS-CBZ-NPs (Table. 3), the size of the NPs and charge over the surface of NPs for TPGS-CBZ-NPs, TPGS-SS-CBZ-NPs, and CTX-TPGS-SS-CBZ-NPs are determined to be 145.6 ± 11.8, 221.6 ± 13.5, and 308.06

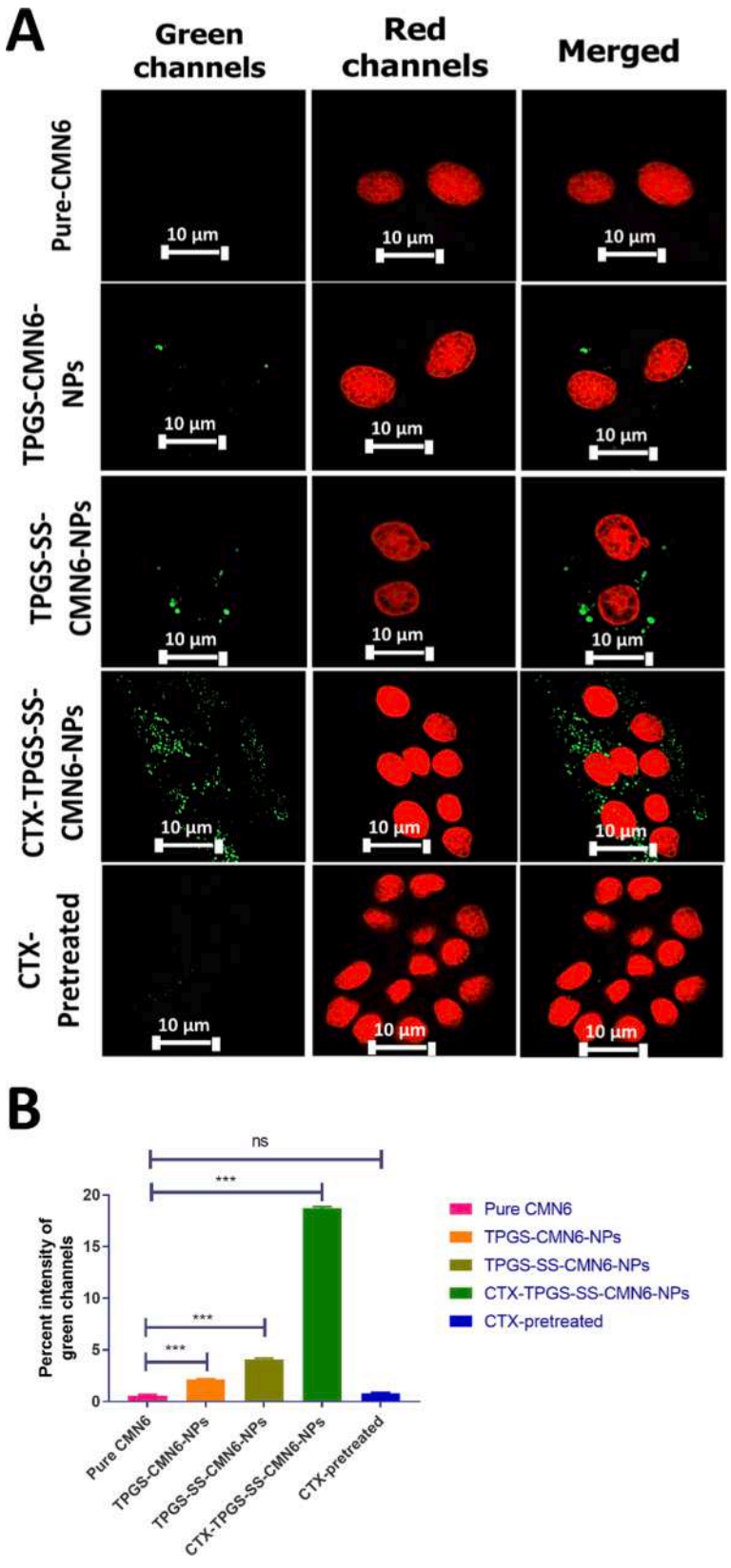

Fig. 9. A) CLSM images show cellular uptake of the free CMN6 (first row), TPGS-CMN6-NPs (second row), TPGS-SS-CMN6-NPs (third row), CTX-TPGS-SS-CMN6-NPs (fourth row), and CTX-pretreated (fifth row) in A549 cells. As shown in the left column (CMN6 channel), CMN6 is distributed in the cytoplasm of A549 cells, the middle column (PI channel) indicates PI stained nuclei, and the right column (merged) depicts CMN6, CMN6 loaded NPs, and PI stained nuclei, respectively, **B)** Graph showing percentage of green fluorescence intensity in A549 cells. (For interpretation of the references to colour in this figure legend, the reader is referred to the web version of this article.)

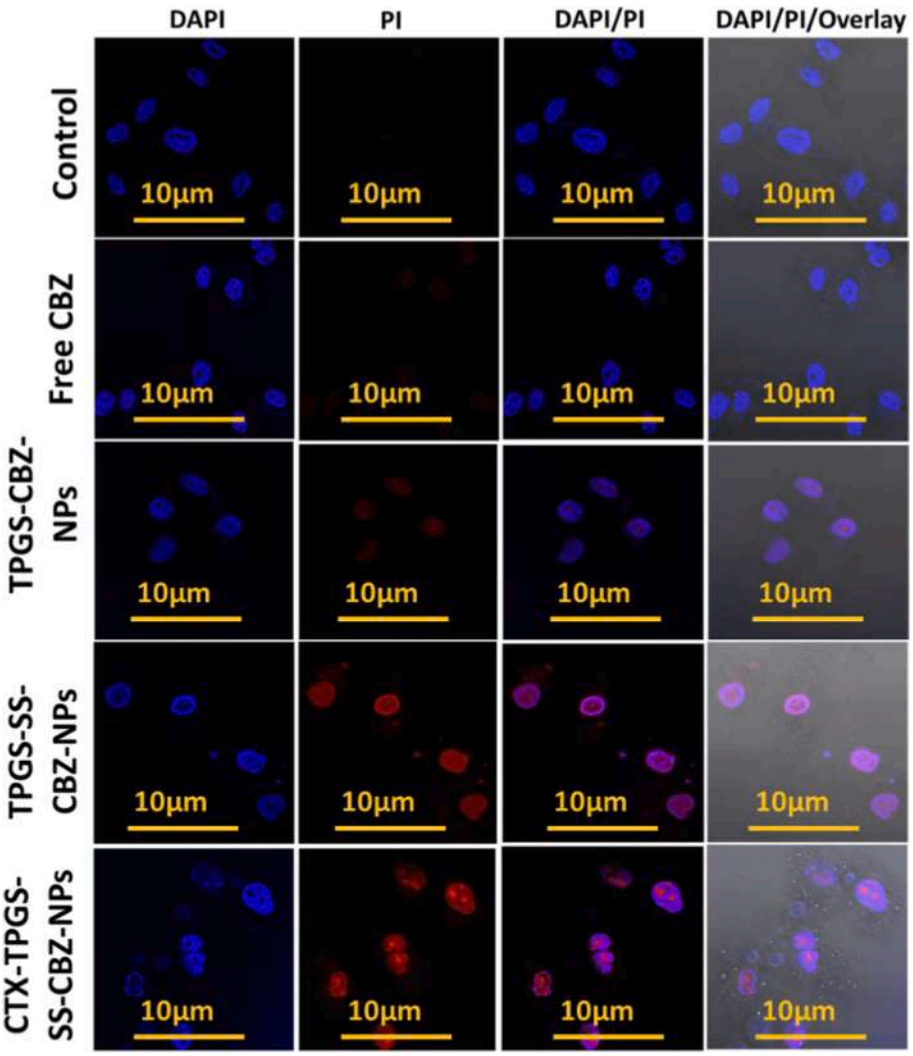

Fig. 10. Changes in the cell morphology after treatment with the free CBZ, TPGS-CBZ-NPs, TPGS-SS-CBZ-NPs, and CTX-TPGS-SS-CBZ-NPs.

± 9.4 nm respectively. The zeta potential of TPGS-CBZ-NPs, TPGS-SS-CBZ-NPs, are determined to be −15 ± 1.42, and −19 ± 2.14, however the CTX-TPGS-SS-CBZ-NPs are determined to be –23 ± 1.96 mV which indicates its better stability. Moreover, the PDI values for TPGS-CBZ-NPs, TPGS-SS-CBZ-NPs, and CTX-TPGS-SS-CBZ-NPs are determined to lie in the range of 0.342 ± 0.083, 0.337 ± 0.072, and 0.336 ± 0.059, which demonstrate that the particles are moderately monodisperse (Table. 3).

3.2.2. *Transmission electron microscopy*

It was used to examine the NPs for information on their size, shape, and morphology. Fig. 4 **I.** shows photographs of NPs at 200 nm scale. Images with a scale of 200 nm, revealed the uniform spheres, with a smooth surfaces.

3.2.3. *Scanning electron microscopy*

Morphological characterization of prepared NPs was carried out using this technique. All of the developed NPs shown in Fig. 4 **II.** were spherical, monodisperse, and smooth, without pinholes or fissures.

3.2.4. *XPS spectroscopy*

Fig. 5 depicts the distinctive peaks in the xps spectra for each of the elements c, o, n, and s. the peaks obtained at binding energies 292–277, 538–525, 408–393, and 160–170 eV were ascribed to C 1 s, O 1 s, N 1 s, and S2p. The percentage of N 1 s, O 1 s, and C 1 s in TPGS-CBZ-NPs, was 76.39 %, 22.65 %, and 0.32 %, respectively, whereas for TPGS-SS-CBZ-NPs these were 76.6 %, 20.61 %, and 1.19 %. Although the atomic percentage of S2p (0.27 %) is present in TPGS-SS-CBZ-NPs, which confirms the presence of sulfur atoms (which belong to the S-S bond) over the surface of NPs. The XPS analysis further confirmed that (CTX) was successfully post-conjugated. The percentage of N 1 s, O 1 s and C 1 s in CTX-TPGS-SS-CBZ-NPs was 72.74 %, 18.04 % and 5.79 %, respectively. However, the peak of the sulfur group is not obtained in CTX-TPGS-SS-CBZ-NPs, which confirms the conjugation of (CTX) over the surface of TPGS-SS-CBZ-NPs.

3.2.5. *XRD spectroscopy*

Analyzing the NPs formulations with XRD revealed the physical state of the NPs. An intense peak at 2 theta value of 24.63° was observed in the pure drug (CBZ), indicating its crystalline nature. However, the TPGS-CBZ-NPs and CTX-TPGS-SS-CBZ-NPs showed sharp peaks at 2 theta values of 16.18°, 24.63°, 29.45°, and 16.98°, 31.60°, respectively. However, the XRD spectra of redox sensitive NPs displayed an amorphous nature **(**Fig.6**).**

3.2.6. *Entrapment efficiency*

For the TPGS-CBZ-NPs, TPGS-SS-CBZ-NPs, and CTX-TPGS-SS-CBZ-NPs, the CBZ entrapment efficiency was determined to be approximately 69.3 ± 3.05, 74.6 ± 2.51, and 79.6 ± 3.05, respectively (Table. 3). Entrapment was aided by the fact that the hydrophobic core of the

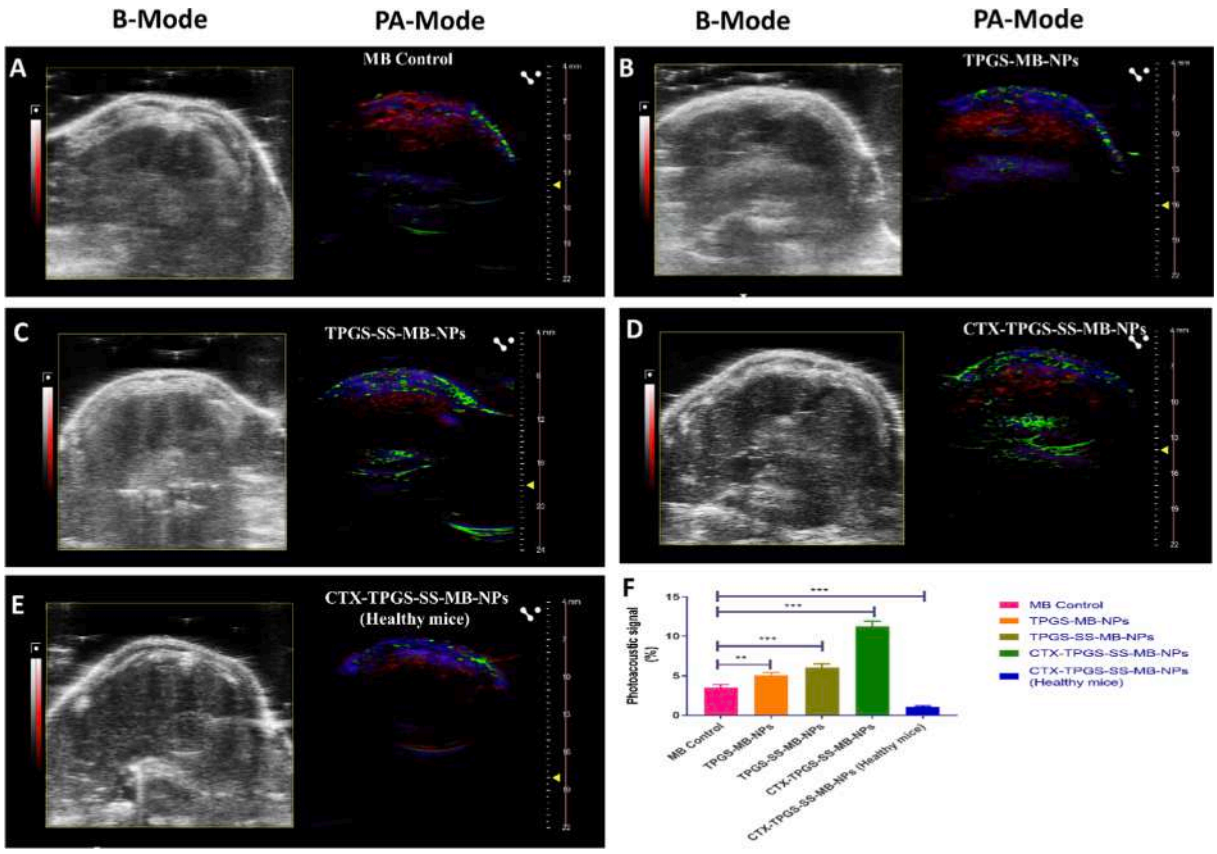

Fig. 11. Images captured by ultrasound and photoacoustic instruments of **(A to D)** mice lungs after an i.v administration of MB-control and MB-loaded NPs into the lungs of cancer-induced mice after 30 min and, **E)** Healthy mice's lungs following a 30-minute intravenous injection of CTX-TPGS-SS-MB-NPs. **F)** histogram depicting the photoacoustic signals.

NPs interacted well with the hydrophobic CBZ. The marginal improvement in the specified nano formulation's entrapment efficiency may be due to the surface decoration of CTX, which resulted in an overall decrease in surface charge. Moreover, the drug loading of TPGS-CBZ-NPs, TPGS-SS-CBZ-NPs, and CTX-TPGS-SS-CBZ-NPs was found to be 7.39, 7.92, and 8.46 % respectively.

3.2.7. *Extent of CTX conjugation*

Bradford assays were performed to determine the extent of CTX conjugated onto the surfaces of TPGS-SS-CBZ-NPs, and over 71 ± 3.127 % of CTX was conjugated.

3.3. *In vitro evaluation*

3.3.1. *In-vitro drug release*

Fig. 7 depicts the results of a 24 h study of drug release at pH (5.5 and 7.4) including two different GSH concentrations (i.e., 5 and 20 mM) for TPGS-CBZ-NPs, TPGS-SS-CBZ-NPs, and CTX-TPGS-SS-CBZ-NPs. At (pH 5.5), 58.1 ± 2.36 %, 66.7 ± 2.14, and 61.7 ± 2.76 % of the medication was released. Moreover, at pH 5.5 with GSH 5 Mm, 69.1 ± 2.92 %, 79.1 ± 3.94 %, and 74.9 ± 1.35 % of the medication were released; at pH 5.5 with GSH 20 mM, this increased to 72.4 ± 1.86 %, 86.6 ± 2.67 %, and 79.3 ± 1.70 % after 24 h. Even though the cumulative drug release at pH 7.4 was found to be 55.78 ± 1.36 %, 63.4 ± 2.57 %, and 58.78 ± 3.14 after 24 h. Although, the drug release observed at pH 7.4 with GSH 5 mM are 63.3 ± 1.80 %, 74.2 ± 2.27 %, and 71.1 ± 1.28 %. However, it increased to 67.3 ± 2.2 %, 81.2 ± 1.36 %, and 76.3 ± 1.21 % at pH 7.4 with GSH 20 mM. The t_{50} values for TPGS-CBZ-NPs at pH 5.5, pH 5.5 + GSH 5 mM, pH 5.5 + GSH 20 mM, pH 7.4, pH 7.4 + GSH 5 mM, and pH 7.4 + GSH 20 mM are determined to be 11.42 ± 0.142, 9.483 ± 0.135, 8.477 ± 0.214, 12.36 ± 0.147, 11.17 ± 0.149, and 9.34 ± 0.156. However, the t_{50} values for TPGS-SS-CBZ-NPs at pH 5.5, pH 5.5 + GSH 5 mM, pH 5.5 + GSH 20 mM, pH 7.4, pH 7.4 + GSH 5 mM, and pH 7.4 + GSH 20 mM are determined to be 5.87 ± 0.123, 4.703 ± 0.126, 3.477 ± 0.145, 10.69 ± 0.214, 9.053 ± 0.254, and 4.343 ± 0.236. Although, the t_{50} CTX-TPGS-SS-CBZ-NPs at pH 5.5, pH 5.5 + GSH 5 mM, pH 5.5 + GSH 20 mM, pH 7.4, pH 7.4 + GSH 5 mM, and pH 7.4 + GSH 20 mM are determined to be 10.36 ± 0.145, 8.043 ± 0.134, 4.463 ± 0.169, 11.75 ± 0.369, 9.712 ± 0.369, and 5.737 ± 0.347 (Table 4). The concept behind disulfide linkage is to ensure that nanoparticles remain intact in the mildly oxidizing extracellular environment. This stability prevents premature dissociation, thereby avoiding the early release of therapeutic agents when the nanoparticles are in the bloodstream. It is possible to quickly re-establish the desired drug release profile once particles enter cells by cleaving disulfide cross-links under reducing conditions (Lai et al., 2014).

The data was displayed using various kinetic equations to examine the mechanism and kinetics of drug release, including zero order, first order, Higuchi's kinetics, and Korsmeyer's equation. In order to analyse the release data, we employed a couple of mathematical models: zero-order kinetics ($Q = k_0 t$), first-order kinetics ($\ln (100\text{-}Q) = \ln Q_0 - k_1 t$), and the Higuchi equation ($Q = k_H t^{1/2}$) to gain insight about the drug release mode from NPs (Muthu and Singh, 2009). Plots with the highest degree of linearity indicated that Higuchi's equation provided the most satisfactory explanation for the *in vitro* drug release. The drug release was found to follow Higuchi's square root of time, according to the examination of the coefficient of determination (r^2), which ranged from 0.9894 to 0.9986. This is because, as shown in Table 5, the r^2 values for Higuchi's square root of time are higher than those for zero-order and first-order kinetics, respectively, which range from 0.7509 to 0.8381 and 0.8877 to 0.9505, respectively. In addition, to comprehend the process of drug release, the data were adjusted according to Peppas

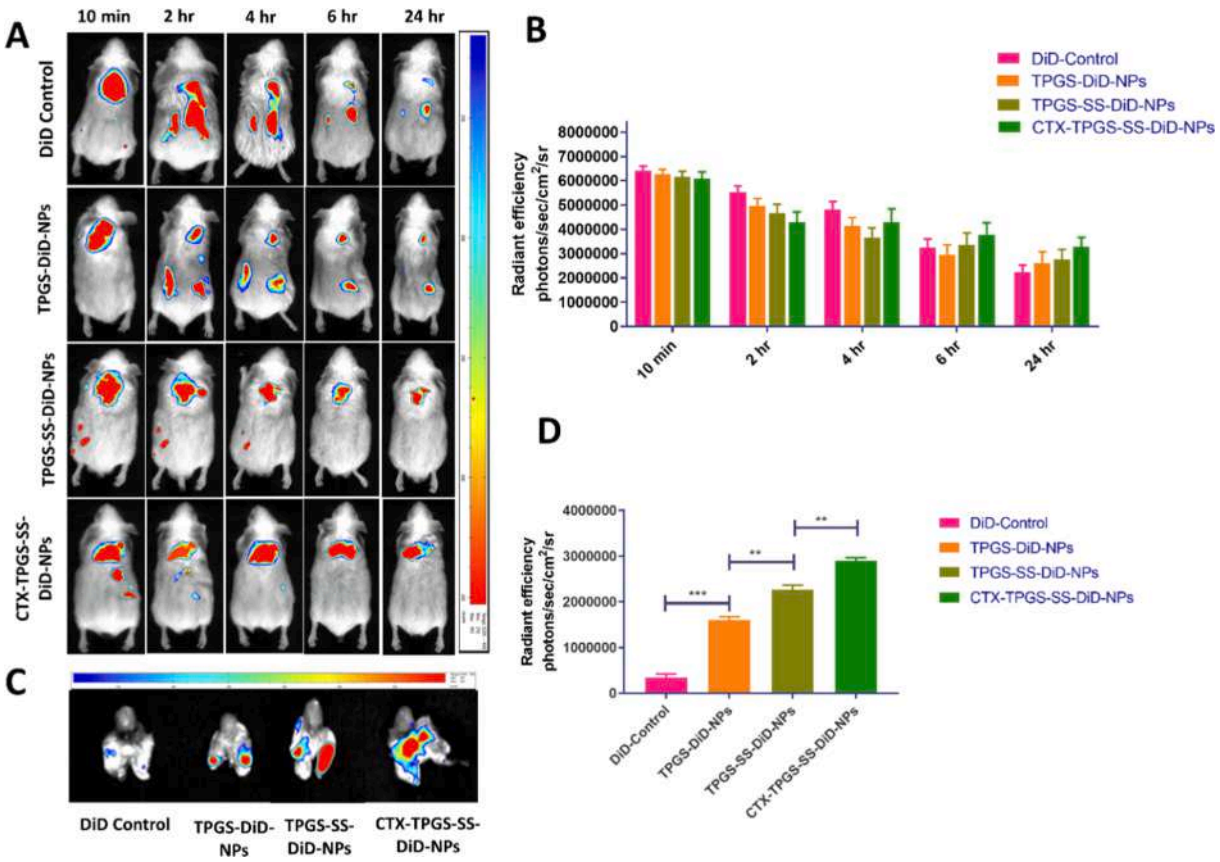

Fig. 12. A) IVIS imaging of DiD control, and DiD loaded-NPs at 10 min, 2 hr, 4 hr, 6 hr, and 24 hr after intravenous administration on B(a)P administered lung carcinoma model, and **B)** graph illustrating the radiant efficiency. **C)** Animals' hearts and lungs that have been extracted after 24 hr of intravenous injection and **D)** graph illustrating the radiant efficiency.

exponential model, denoted as $Mt/M\infty = Kt^n$. In this model, 't' represents the fraction of the drug released after time 't,' 'K' stands for the kinetic constant, and 'n' is the release exponent that defines the drug transport mechanism. The drug releases were further indicated by the values 'n' being in the range of 0.380 to 0.531, which is consistent with the Quasi Fickian diffusion control mechanism (Table 5).

Polymeric micellar NPs have the potential to encapsulate pharmaceuticals and release them in a regulated manner, making them attractive candidates for drug delivery. Drug release from micelles can occur through both diffusion and disintegration from intact NPs. In Higuchi's model, the square root of the drug release from an insoluble matrix describes a process that changes over time and is based on Fickian diffusion (Paarakh et al., 2018). This explains the phenomenon known as square root kinetics, or Higuchi's kinetics, where the medication diffuses at a somewhat slower pace as the diffusion distance increases (Mohammadi et al., 2023).

3.3.2. *In-vitro cytotoxicity study*

The data show that, compared to the CBZ control, cytotoxicity produced by the TPGS-CBZ-NPs, TPGS-SS-CBZ-NPs, and CTX-TPGS-SS-CBZ-NPs is a tremendous exaggeration (Fig. 8). The data obtained demonstrates that at lower concentrations, the viability of cells is not significantly affected by CBZ control. The IC_{50} value of CBZ were found at 17.54 ± 3.58 μg/ml while TPGS-CBZ-NPs, were found at 12.80 ± 2.45 μg/ml while TPGS-SS-CBZ-NPs, shows 9.28 ± 1.13 μg/ml, and the CTX-TPGS-SS-CBZ-NPs was found most effective as 4.013 ± 1.05 μg/ml **(**Fig. 8**A).** Targeted CBZ delivery to A549 cells, where the EGFR receptor is overexpressed, can significantly improve the drug's anticancer efficacy. However, the encapsulation in either a TPGS-CBZ-NPs or TPGS-SS-CBZ-NPs system increases their efficacy by 1.37 and 1.89 folds, respectively, in A549 cells. Furthermore, the efficiency of NPs drugs is increased by a factor of 4.37 folds when they are delivered via receptor-mediated drug delivery (i.e., CTX-TPGS-SS-CBZ-NPs) **(**Fig. 8**B).**

3.3.3. *In vitro cellular uptake study*

Images of CMN6-loaded NPs and pure CMN6 as well as merged images were captured to illustrate their uptake into cells. Endocytosis of CMN6-loaded formulations is shown in green, and the nucleus is shown in red. A measure of the prevalence of green channels in the cellular uptake was performed with Image-J **(**Fig. 9**B).** There was a total of 0.598 ± 0.086 % of pure CMN6, 2.11 ± 0.04 % of TPGS- CMN6 -NPs, 4.096 ± 0.120 % of TPGS-SS- CMN6 -NPs, 18.713 ± 0.167 % of CTX-TPGS-SS-CMN6 -NPs, and 0.799 ± 0.094 % of CTX-pretreated. Green channels are more prevalent in receptor-targeted NPs than in pure CMN6 ($p < 0.001$), but they are also more prevalent in TPGS-CMN6-NPs and TPGS-SS-CMN6-NPs. Confocal micrographs depicting the uptake of pure CMN6, TPGS-CMN6-NPs, TPGS-SS-CMN6-NPs, and CTX-TPGS-SS-CMN6 -NPs by A549 cell lines *in-vitro* are shown in Fig 9**A**. These images show that compared to TPGS- CMN6 -NPs and pure CMN6, TPGS-SS-CMN6-NPs, and CTX-TPGS-SS-CMN6-NPs significantly increase the confocal intensity produced by A549 cells. Since EGF receptors showed an endocytic pathway, the dramatic increase in CTX-TPGS-SS-CMN6-NPs uptake in A549 cells is plausible (via-caveolae). After incubation with CTX-TPGS-SS-CMN6-NPs, cells that were pretreated with CTX showed significantly reduced confocal fluorescence.

3.3.4. *DAPI/PI staining for apoptosis*

An investigation of DAPI and PI colocalization using CLSM was carried out to provide further evidence that the impact on cell viability was caused by apoptosis produced by the free drug and

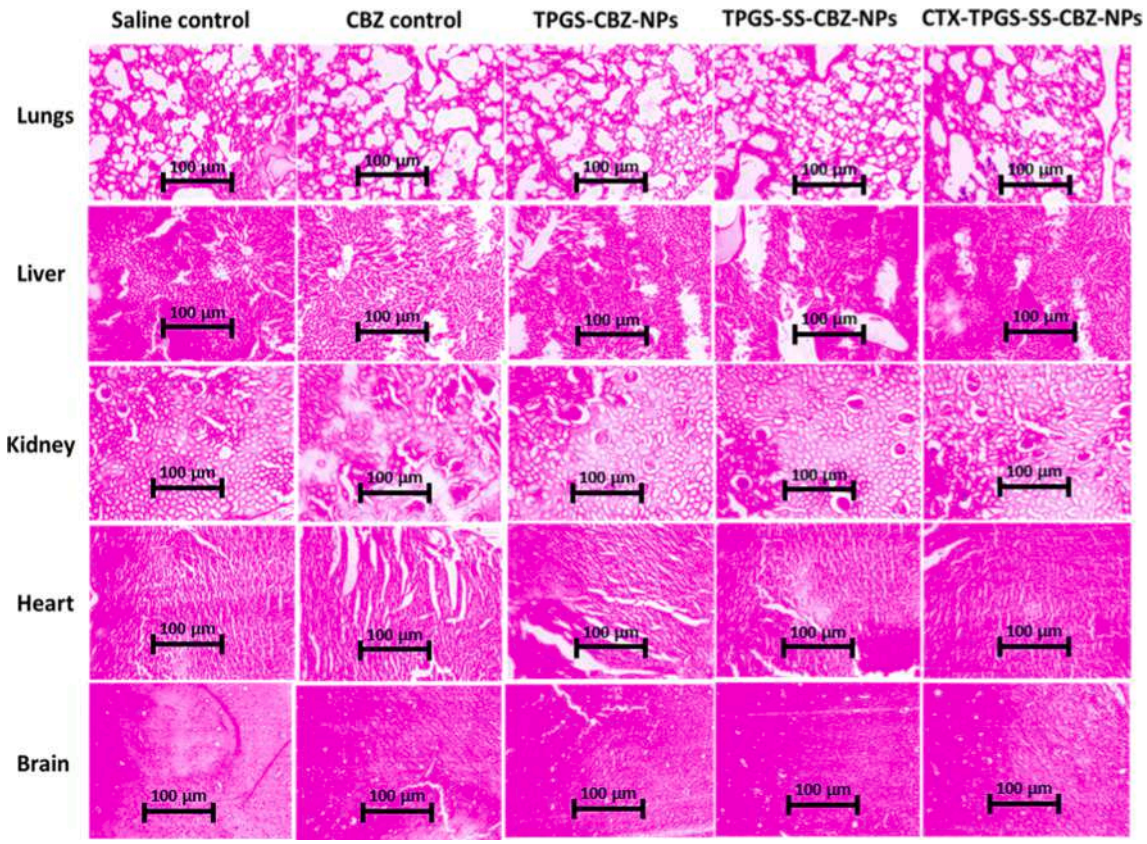

Fig. 13. Histopathological images of the rat's vital organs after treatments with saline control, CBZ control, TPGS-CBZ-NPs, TPGS-SS-CBZ-NPs, and CTX-TPGS-SS-CBZ-NPs.

nanoformulations distribution into the cytoplasm. As part of this research, we stained cell nuclei with DAPI and PI following treatment with free CBZ, TPGS-CBZ-NPs, TPGS-SS-CBZ-NPs, and CTX-TPGS-SS-CBZ-NPs. The PI stains compacted and fragmented chromatin depending on nuclear fragmentation, whereas DAPI stains the cellular nucleus. As a result, cells that co-localize DAPI and PI following incubation with CTX-TPGS-SS-CBZ-NPs are confirmed to be dead cells. When exposed to free drug or other nano formulations, however, very few cells display PI and DAPI colocalization, and even fewer cells exhibit strong PI staining. In addition, compared to the free drug and other nano formulations, CTX-TPGS-SS-CBZ-NPs showed a greater number of apoptotic cells in A549 cells **(**Fig 10**).**

3.4. In vivo evaluation

3.4.1. Lung biodistribution of nanomedicine in mice via ultrasound/ photoacoustic imaging

After 30 min of intravenous (i.v) administration, the *in vivo* distribution of the MB-loaded NPs and MB control was visualized using photoacoustic images of the lungs of the animals **(**Fig. 11**A-D)**. The presence of the NPs was revealed by green photoacoustic signals. B(a)P induce model treated with MB control, TPGS-MB-NPs, TPGS-SS-MB-NPs, and CTX-TPGS-SS-MB-NPs showed photoacoustic signal intensities in the lung areas of 3.544 ± 0.345 %, 5.064 ± 0.367 %, 6.076 ± 0.145 %, and 11.238 ± 0.697 %, respectively. In contrast, CTX-TPGS-SS-MB-NPs resulted in a percentage of photoacoustic signals of 1.053 ± 0.1450 % in healthy mice **(**Fig. 11**E)**. It is possible to infer the distribution of MB and MB-loaded NPs in the body by analysing the fraction of photoacoustic signals **(**Fig. 11**F)** Based on the results of the study, CTX-TPGS-SS-MB-NPs showed greater photoacoustic signals than MB control and MB loaded formulations ($p < 0.001$).

3.4.2. Targeting lungs by live imaging with IVIS

Mice injected with B(a)P were imaged with IVIS in real-time using DiD-control and DiD-loaded NPs. Radiant efficiency, measured as the intensity of fluorescence per unit area per unit time, was compared across different time points and treatment groups using the Tukey's test. At 10 min post-injection, mice treated with DiD control found no discernible variations in radiant efficiency compared to mice treated with DiD-loaded-NPs. After 2 hr post-injection, the radiant efficiency decreased in each of the groups receiving therapy; in comparison to the mice with DiD control, the TPGS-DiD-NPs did not show any significant difference, while the TPGS-SS-DiD-NPs and CTX-TPGS-SS-DiD-NPs showed a significant increase. After 24 hr of post-injection, the DiD control-treated animal's lung radiant efficiency was lower than that of the TPGS-DiD-NPs treated animal **(**Fig. 12**A)**. Although in the case of TPGS-SS-DiD-NPs provides a higher radiant efficiency signal as compared to TPGS-DiD-NPs. Moreover, CTX-TPGS-SS-DiD-NPs provided a larger radiant efficiency signal in comparison to the DiD control, TPGS-DiD-NPs, TPGS-SS-DiD-NPs, and CTX-TPGS-SS-DiD-NPs **(**Fig. 12**B)**. Furthermore, after 24 hr we harvested the lungs of animals that were treated with DiD control, TPGS-DiD-NPs, TPGS-SS-DiD-NPs, and CTX-TPGS-SS-DiD-NPs **(**Fig. 12**C)**. It has been shown that in DiD control, the radiant efficiency signal was lesser as compared to the CTX-TPGS-SS-DiD-NPs. Fig. 12**D** shows a statistically significant difference between DiD-control, TPGS-DiD-NPs, TPGS-SS-DiD-NPs, and CTX-TPGS-SS-DiD-NPs with a p-value less than 0.001 ($p < 0.001$).

3.4.3. Histopathology analysis

The lungs, liver, kidneys, heart, and brain were extracted from animals that had received free CBZ, TPGS-CBZ-NPs, TPGS-SS-CBZ-NPs, and CTX-TPGS-SS-CBZ-NPs at a dose of 6.5 mg/kg, and then subjected to H & E staining. The organ specimen was examined under a microscope, and the resulting images are shown in Fig. 13**.** To determine, if any of the NPs

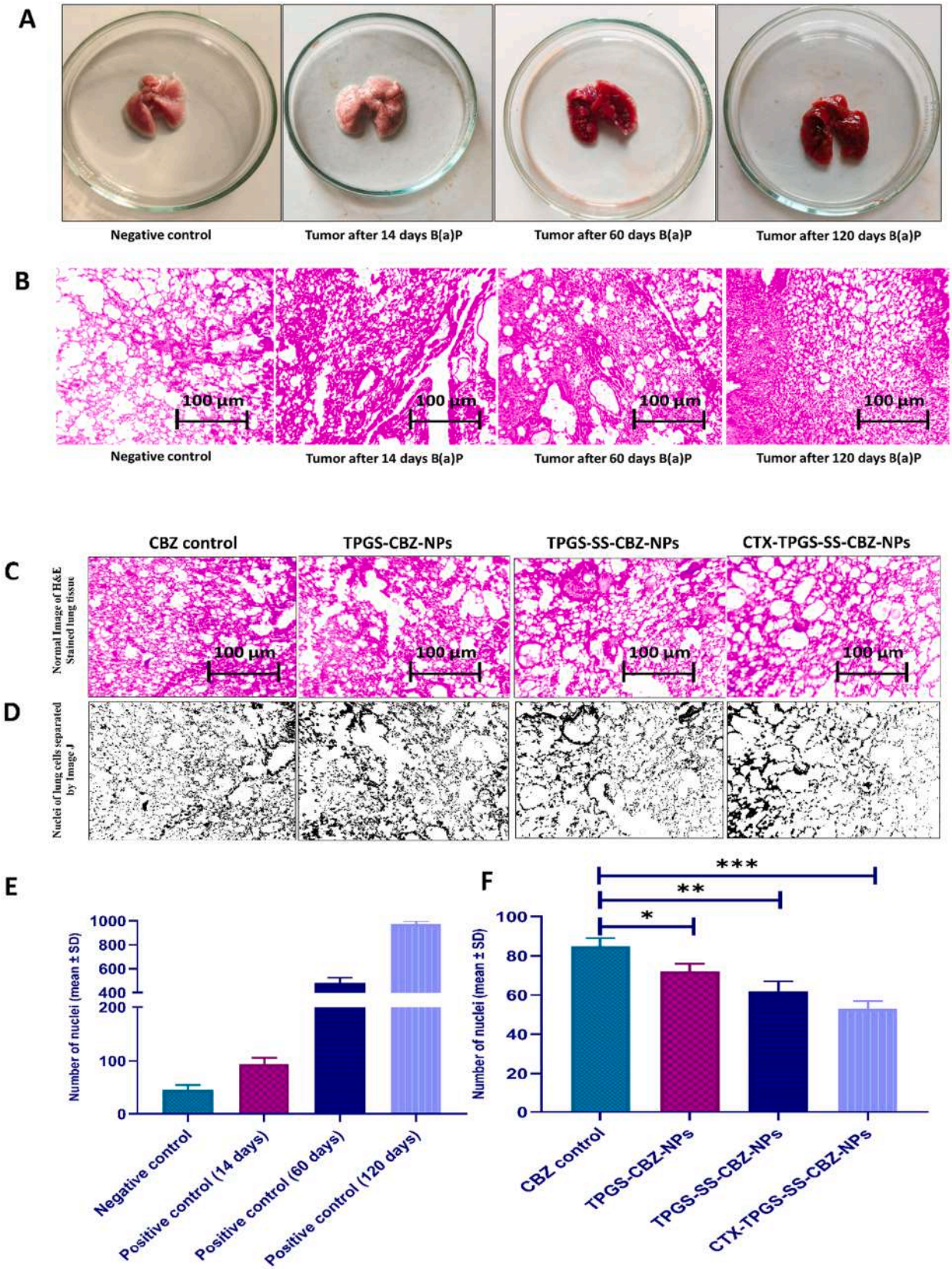

Fig. 14. **A)** Images of mice lungs; **B)** Histopathological H&E staining of mice lungs; **C)** H&E staining of respective treatment groups; **D)** Nuclei of lung cells separated through Image J; **E)** Graph showing the number of nuclei of B(a)P administered lung carcinoma; **F)** Graph illustrating the relative *in-vivo* tumour inhibition by CBZ control, TPGS-CBZ-NPs, TPGS-SS-CBZ-NPs, CTX-TPGS-SS-CBZ-NPs ***P < 0.0001, *P < 0.05).

formulations were harmful, histopathology pictures of CBZ-control and NPs-treated rats were examined. In the CBZ control group, no pathological abnormalities were seen in any of the vital organs, as evidenced by the histology study. Histopathological pictures show that the drug's safety profile is marginally better in nontargeted NPs. Moreover, targeted NPs did not cause any toxicity in the essential organs, and the resulting images were identical to those seen in the control group.

3.4.4. *In vivo anticancer efficacy*

Fig. 14 shows the processed pictures of stained slices of histology using H&E of a B(a)P administered lung carcinoma model following a course of treatment with saline control, CBZ control, TPGS-CBZ-NPs, TPGS-SS-CBZ-NPs, and CTX-TPGS-SS-CBZ-NPs. Here, the nucleus and cytoplasm were separated using the ImageJ software, so that the quantitative evaluation of lung cancer after therapies could proceed. After the given amount of time had passed during treatments, the H&E sections were examined using the ImageJ software. The lung cancer nuclei counting was done by ImageJ software. The statistical significance of the data were determined by a one-way ANOVA ($P < 0.05$).

4. Conclusion

CBZ loaded CTX functionalised novel redox sensitive TPGS based NPs was developed for EGFR targeted delivery to NSCLC. The thiolated TPGS was prepared and evaluated by FTIR and NMR spectroscopy. Physicochemical characteristics, *in vitro*, and *in vivo* analysis were conducted on the developed formulations. Particle entrapment efficiency, size, charge, and polydispersity all fall within acceptable ranges. The XPS analysis confirmed that cetuximab coats the surface of the redox-sensitive NPs. The GSH levels are related to drug release, which follows from studies conducted *in vitro* at pH 5.5 and 7.4 where *in vivo* redox potentials of > 20 mM are evident in cancer microenvironments. Cancer selectivity was confirmed by an MTT experiment, and the involvement of EGF receptors in actively targeted administration with subsequent prompted release of CBZ due to its redox-sensitive properties was approved. It has been demonstrated that targeted NPs are more cytotoxic *in vitro*. Increased uptake of CMN6-loaded CTX-decorated redox-sensitive NPs was demonstrated in *in vitro* cellular uptake tests compared to uptake of free CMN6 and nontargeted NPs. However, in comparison to alternative NPs, the targeted redox-sensitive NPs showed significantly greater anticancer activity and prolonged longevity in a mice model of lung tumour development. Alternatively, a B(a)P administered lung carcinoma model showed better targeting in the lungs when formulations contains DiD dye as the fluorescent material were imaged in real time using IVIS, and enhanced lung biodistribution for EGFR-targeted redox-sensitive NPs was demonstrated using ultrasound/photoacoustic imaging with MB as a contrast agent. Also, the histopathology study confirmed that the NPs were safe to use. According to *in-vivo* tumour reduction experimental work conducted on B(a)P-administered lung carcinoma model concluded that targeted redox sensitive NPs significantly reduces cell number compared to non-targeted NPs, and formulations prove to be more effective against cancer than the CBZ control. After further clinical validation, the redox-sensitive TPGS-SS nanomedicines show promise as candidates for the administration of antineoplastic medications.

CRediT authorship contribution statement

Aseem Setia: Conceptualization, Investigation, Methodology. **Pooja Kumari:** Visualization. **Vikas:** Data curation, Methodology, Validation. **Abhishesh Kumar Mehata:** Formal analysis, Methodology, Writing – original draft, Writing – review & editing. **Ankit Kumar Malik:** Formal analysis, Methodology. **Sanjeev Kumar Mahto:** Validation, Visualization. **Madaswamy S. Muthu:** Conceptualization, Investigation, Methodology, Project administration, Supervision, Writing – review & editing.

Declaration of competing interest

The authors declare that they have no known competing financial interests or personal relationships that could have appeared to influence the work reported in this paper.

Data availability

Data will be made available on request.

Acknowledgements

The authors are grateful to the ICMR (Govt of India) for granting project. Project No. 35/8/2020-Nano/BMS. In addition, the authors are grateful to the Central Instrument Facilities (CIF) at IIT-BHU in Varanasi for providing them with the necessary equipment facilities. We also want to thank SATHI-BHU for providing an Ultrasound and Photoacoustic imaging facility.

References

Agarwal, M., Agarwal, M.K., Shrivastav, N., Pandey, S., Das, R., Gaur, P., 2018. Preparation of chitosan nanoparticles and their in-vitro characterization. Int. J. Life-Sci. Sci. Res. 4, 1713–1720.

Alberg, A.J., Brock, M.V., Ford, J.G., Samet, J.M., Spivack, S.D., 2013. Epidemiology of lung cancer: Diagnosis and management of lung cancer, 3rd ed: American College of Chest Physicians evidence-based clinical practice guidelines. Chest 143, e1S-e29S.

Alberts, B., 2017. Molecular biology of the cell. Garland science.

Alexandrov, K., Rojas, M., Satarug, S., 2010. The critical DNA damage by benzo(a)pyrene in lung tissues of smokers and approaches to preventing its formation. Toxicol. Lett. 198, 63–68.

Antoniou, J., Liu, F., Majeed, H., Qi, J., Yokoyama, W., Zhong, F., 2015. Physicochemical and morphological properties of size-controlled chitosan–tripolyphosphate nanoparticles. Colloids Surf. A: Physicochem. Eng. Asp 465, 137–146.

Appel, B.R., Guirguis, G., Kim, I.S., Garbin, O., Fracchia, M., Flessel, C.P., Kizer, K.W., Book, S.A., Warriner, T.E., 1990. Benzene, benzo(a)pyrene, and lead in smoke from tobacco products other than cigarettes. Am. J. Public Health 80, 560–564.

Cafaggi, S., Russo, E., Stefani, R., Leardi, R., Caviglioli, G., Parodi, B., Bignardi, G., De Totero, D., Aiello, C., Viale, M., 2007. Preparation and evaluation of nanoparticles made of chitosan or N-trimethyl chitosan and a cisplatin-alginate complex. J. Control Release 121, 110–123.

Cao, H., Zhang, Z., Zhao, S., He, X., Yu, H., Yin, Q., Zhang, Z., Gu, W., Chen, L., Li, Y., 2015. Hydrophobic interaction mediating self-assembled nanoparticles of succinobucol suppress lung metastasis of breast cancer by inhibition of VCAM-1 expression. J. Control Release 205, 162–171.

Chaudhary, M.R., Chaudhary, S., Sharma, Y., Singh, T.A., Mishra, A.K., Sharma, S., Mehdi, M.M., 2023. Aging, oxidative stress and degenerative diseases: mechanisms, complications and emerging therapeutic strategies. Biogerontology 24, 609–662.

Cheng, R., Feng, F., Meng, F., Deng, C., Feijen, J., Zhong, Z., 2011. Glutathione-responsive nano-vehicles as a promising platform for targeted intracellular drug and gene delivery. J. Control Release 152, 2–12.

Crucho, C.I., 2015. Stimuli-responsive polymeric nanoparticles for nanomedicine. ChemMedChem 10, 24–38.

Eskra, J.N., Dodge, A., Bosland, M.C., 2016. Microtubule polymerizing effects of ellagic acid reduce efficacy of taxane chemotherapy. Cancer Res. 76, 317.

Gill, K.K., Kaddoumi, A., Nazzal, S., 2012. Mixed micelles of PEG(2000)-DSPE and vitamin-E TPGS for concurrent delivery of paclitaxel and parthenolide: enhanced chemosenstization and antitumor efficacy against non-small cell lung cancer (NSCLC) cell lines. Eur. J. Pharm. Sci. 46, 64–71.

Housman, G., Byler, S., Heerboth, S., Lapinska, K., Longacre, M., Snyder, N., Sarkar, S., 2014. Drug resistance in cancer: an overview. Cancers (Basel) 6, 1769–1792.

Hu, X., Geetha, R.V., Surapaneni, K.M., Veeraraghavan, V.P., Chinnathambi, A., Alahmadi, T.A., Manikandan, V., Manokaran, K., 2021. Lung cancer induced by Benzo(A)Pyrene: ChemoProtective effect of sinapic acid in swiss albino mice. Saudi J. Biol. Sci. 28, 7125–7133.

Jha, A., Viswanadh, M.K., Burande, A.S., Mehata, A.K., Poddar, S., Yadav, K., Mahto, S. K., Parmar, A.S., Muthu, M.S., 2020. DNA biodots based targeted theranostic nanomedicine for the imaging and treatment of non-small cell lung cancer. Int. J. Biol. Macromol. 150, 413–425.

Jiang, P., Liang, B., Zhang, Z., Fan, B., Zeng, L., Zhou, Z., Mao, Z., Xu, Q., Yao, W., Shen, Q., 2023. New insights into nanosystems for non-small-cell lung cancer: diagnosis and treatment. RSC Adv. 13, 19540–19564.

Jithan, A., Madhavi, K., Madhavi, M., Prabhakar, K., 2011. Preparation and characterization of albumin nanoparticles encapsulating curcumin intended for the treatment of breast cancer. Int. J. Pharm. Investig. 1, 119–125.

John, K., Pratt, M.M., Beland, F.A., Churchwell, M.I., McMullen, G., Olivero, O.A., Pogribny, I.P., Poirier, M.C., 2012. Benzo [a] pyrene (BP) DNA adduct formation in DNA repair–deficient p53 haploinsufficient [Xpa (−/−) p53 (+/−)] and wild-type mice fed BP and BP plus chlorophyllin for 28 days. Carcinogenesis 33, 2236–2241.

Karavelioglu, E., Gonul, Y., Aksit, H., Boyaci, M.G., Karademir, M., Simsek, N., Guven, M., Atalay, T., Rakip, U., 2016. Cabazitaxel causes a dose-dependent central nervous system toxicity in rats. J. Neurol. Sci. 360, 66–71.
Katakami, N., Tada, H., Mitsudomi, T., Kudoh, S., Senba, H., Matsui, K., Saka, H., Kurata, T., Nishimura, Y., Fukuoka, M., 2012. A phase 3 study of induction treatment with concurrent chemoradiotherapy versus chemotherapy before surgery in patients with pathologically confirmed N2 stage IIIA nonsmall cell lung cancer (WJTOG9903). Cancer 118, 6126–6135.
Kennedy, L., Sandhu, J.K., Harper, M.E., Cuperlovic-Culf, M., 2020. Role of glutathione in cancer: from mechanisms to therapies. Biomolecules 10.
Kommineni, N., Mahira, S., Domb, A.J., Khan, W., 2019. Cabazitaxel-loaded nanocarriers for cancer therapy with reduced side effects. Pharmaceutics 11.
Kumari, S., Badana, A.K., G, M.M., G, S., Malla, R., 2018. Reactive Oxygen Species: A Key Constituent in Cancer Survival. Biomark Insights 13, 1177271918755391.
Kutty, R.V., Feng, S.S., 2013. Cetuximab conjugated vitamin E TPGS micelles for targeted delivery of docetaxel for treatment of triple negative breast cancers. Biomaterials 34, 10160–10171.
Lai, T.C., Cho, H., Kwon, G.S., 2014. Reversibly core cross-linked polymeric micelles with pH-and reduction-sensitivities: effects of cross-linking degree on particle stability, drug release kinetics, and anti-tumor efficacy. Polym. Chem. 5, 1650–1661.
Łazar-Poniatowska, M., Bandura, A., Dziadziuszko, R., Jassem, J., 2021. Concurrent chemoradiotherapy for stage III non-small-cell lung cancer: recent progress and future perspectives (a narrative review). Transl. Lung Cancer Res. 10, 2018–2031.
Lemjabbar-Alaoui, H., Hassan, O.U., Yang, Y.W., Buchanan, P., 2015. Lung cancer: Biology and treatment options. Biochim. Biophys. Acta 1856, 189–210.
Lian, H., He, Z., Meng, Z., 2017. Rational design of hybrid nanomicelles integrating mucosal penetration and P-glycoprotein inhibition for efficient oral delivery of paclitaxel. Colloids Surf. B Biointerfaces 155, 429–439.
Mahmood, M.Q., Ward, C., Muller, H.K., Sohal, S.S., Walters, E.H., 2017. Epithelial mesenchymal transition (EMT) and non-small cell lung cancer (NSCLC): a mutual association with airway disease. Med. Oncol. 34, 45.
Mazzarella, L., Guida, A., Curigliano, G., 2018. Cetuximab for treating non-small cell lung cancer. Expert Opin. Biol. Ther. 18, 483–493.
Meza, R., Meernik, C., Jeon, J., Cote, M.L., 2015. Lung cancer incidence trends by gender, race and histology in the United States, 1973–2010. PLoS One 10, e0121323.
Mohammadi, F., Moradi, A., Tavakoli, F., Rahmati, S., Giti, R., Ramezani, V., 2023. Development and characterization of a copolymeric micelle containing soluble and insoluble model drugs. PLoS One 18, e0286251.
Molina, J.R., Yang, P., Cassivi, S.D., Schild, S.E., Adjei, A.A., 2008. Non-small cell lung cancer: epidemiology, risk factors, treatment, and survivorship. Mayo Clin. Proc. 83, 584–594.
Morales-Cruz, M., Cruz-Montañez, A., Figueroa, C.M., González-Robles, T., Davila, J., Inyushin, M., Loza-Rosas, S.A., Molina, A.M., Muñoz-Perez, L., Kucheryavykh, L.Y., Tinoco, A.D., Griebenow, K., 2016. Combining stimulus-triggered release and active targeting strategies improves cytotoxicity of cytochrome c nanoparticles in tumor cells. Mol. Pharm. 13, 2844–2854.
Muthu, M.S., Kulkarni, S.A., Liu, Y., Feng, S.S., 2012. Development of docetaxel-loaded vitamin E TPGS micelles: formulation optimization, effects on brain cancer cells and biodistribution in rats. Nanomedicine (Lond.) 7, 353–364.
Muthu, M.S., Kutty, R.V., Luo, Z., Xie, J., Feng, S.S., 2015. Theranostic vitamin E TPGS micelles of transferrin conjugation for targeted co-delivery of docetaxel and ultra bright gold nanoclusters. Biomaterials 39, 234–248.
Muthu, M.S., Singh, S., 2009. Poly (D, L-lactide) nanosuspensions of risperidone for parenteral delivery: formulation and in-vitro evaluation. Curr. Drug Deliv. 6, 62–68.
Nomier, Y.A., Alshahrani, S., Elsabahy, M., Asaad, G.F., Hassan, A., El-Dakroury, W.A., 2022. Ameliorative effect of chitosan nanoparticles against carbon tetrachloride-induced nephrotoxicity in Wistar rats. Pharm. Biol. 60, 2134–2144.
Paarakh, M.P., Jose, P.A., Setty, C.M., Peterchristoper, G., 2018. Release kinetics–concepts and applications. Int. J. Pharm. Res. Tech. 8, 12–20.
Pooja, D., Babu Bikkina, D.J., Kulhari, H., Nikhila, N., Chinde, S., Raghavendra, Y.M., Sreedhar, B., Tiwari, A.K., 2014. Fabrication, characterization and bioevaluation of silibinin loaded chitosan nanoparticles. Int. J. Biol. Macromol. 69, 267–273.
Rani, S., Sahoo, R.K., Kumar, V., Chaurasiya, A., Kulkarni, O., Mahale, A., Katke, S., Kuche, K., Yadav, V., Jain, S., Nakhate, K.T., Ajazuddin, Gupta, U., 2023. N-2-Hydroxypropylmethacrylamide-polycaprolactone polymeric micelles in co-delivery of proteasome inhibitor and polyphenol: exploration of synergism or antagonism. Mol Pharm 20, 524-544.
Rodic, S., Vincent, M.D., 2018. Reactive oxygen species (ROS) are a key determinant of cancer's metabolic phenotype. Int. J. Cancer 142, 440–448.
Rugamba, A., Kang, D.Y., Sp, N., Jo, E.S., Lee, J.M., Bae, S.W., Jang, K.J., 2021. Silibinin regulates tumor progression and tumorsphere formation by suppressing PD-L1 expression in non-small cell lung cancer (NSCLC) cells. Cells 10.
Santos, E.D.S., Nogueira, K.A.B., Fernandes, L.C.C., Martins, J.R.P., Reis, A.V.F., Neto, J. B.V., Júnior, I., Pessoa, C., Petrilli, R., Eloy, J.O., 2021. EGFR targeting for cancer therapy: Pharmacology and immunoconjugates with drugs and nanoparticles. Int. J. Pharm. 592, 120082.
Schluger, N.W., Koppaka, R., 2014. Lung disease in a global context. A call for public health action. Ann. Am. Thorac. Soc. 11, 407–416.
Shen, C., Zhu, J., Song, J., Wang, J., Shen, B., Yuan, H., Li, X., 2020. Formulation of pluronic F127/TPGS mixed micelles to improve the oral absorption of glycyrrhizic acid. Drug Dev. Ind. Pharm. 46, 1100–1107.
Society, A.C., 2021. Key Statistics for Lung Cancer. 2023. https://www.cancer.org/cancer/types/lung-cancer/about/key-statistics.html.
Stinchcombe, T.E., Bogart, J., Veeramachaneni, N.K., Kratzke, R., Govindan, R., 2011. Annual review of advances in non-small cell lung cancer research: a report for the year 2010. J. Thorac. Oncol. 6, 1443–1450.
Sun, Q., Luan, L., Arif, M., Li, J., Dong, Q.J., Gao, Y., Chi, Z., Liu, C.G., 2018. Redox-sensitive nanoparticles based on 4-aminothiophenol-carboxymethyl inulin conjugate for budesonide delivery in inflammatory bowel diseases. Carbohydr. Polym. 189, 352–359.
Sung, H., Ferlay, J., Siegel, R.L., Laversanne, M., Soerjomataram, I., Jemal, A., Bray, F., 2021. Global cancer statistics 2020: GLOBOCAN estimates of incidence and mortality worldwide for 36 cancers in 185 countries. CA Cancer J. Clin. 71, 209–249.
Tao, M.-H., Imaging, 2019. Epidemiology of lung cancer. Lung Cancer 4-1-4-15.
Travis, W.D., 2012. Update on small cell carcinoma and its differentiation from squamous cell carcinoma and other non-small cell carcinomas. Mod. Pathol. 25 (Suppl 1), S18–S30.
Van Meir, E.G., Hadjipanayis, C.G., Norden, A.D., Shu, H.K., Wen, P.Y., Olson, J.J., 2010. Exciting new advances in neuro-oncology: the avenue to a cure for malignant glioma. CA Cancer J. Clin. 60, 166–193.
Vikas, Mehata, A.K., Viswanadh, M.K., Malik, A.K., Setia, A., Kumari, P., Mahto, S.K., Muthu, M.S., 2023. EGFR Targeted Redox Sensitive Chitosan Nanoparticles of Cabazitaxel: Dual-Targeted Cancer Therapy, Lung Distribution, and Targeting Studies by Photoacoustic and Optical Imaging. Biomacromolecules 24, 4989-5003.
Viswanadh, M.K., Agrawal, N., Azad, S., Jha, A., Poddar, S., Mahto, S.K., Muthu, M.S., 2021. Novel redox-sensitive thiolated TPGS based nanoparticles for EGFR targeted lung cancer therapy. Int. J. Pharm. 602, 120652.
Wang, T., Nelson, R.A., Bogardus, A., Grannis Jr., F.W., 2010. Five-year lung cancer survival: which advanced stage nonsmall cell lung cancer patients attain long-term survival? Cancer 116, 1518–1525.
Xu, X., Wu, H., Yang, Y., Liu, B., Tian, J., Bao, H., Liu, T., 2022. PLGA-coated methylene blue nanoparticles for photoacoustic imaging and photodynamic/photothermal cascaded precisely synergistic therapy of tumor. RSC Adv. 12, 1543–1549.
Xue, P., Liu, D., Wang, J., Zhang, N., Zhou, J., Li, L., Guo, W., Sun, M., Han, X., Wang, Y., 2016. Redox-sensitive citronellol-cabazitaxel conjugate: Maintained in vitro cytotoxicity and self-assembled as multifunctional nanomedicine. Bioconjug. Chem. 27, 1360–1372.
Yang, X., Cai, X., Yu, A., Xi, Y., Zhai, G., 2017. Redox-sensitive self-assembled nanoparticles based on alpha-tocopherol succinate-modified heparin for intracellular delivery of paclitaxel. J. Colloid Interface Sci. 496, 311–326.
Zappa, C., Mousa, S.A., 2016. Non-small cell lung cancer: current treatment and future advances. Transl. Lung Cancer Res. 5, 288–300.
Zhang, J.M., Zhang, M.R., Yang, C.H., Li, Y., 2022. The meaning of life according to patients with advanced lung cancer: a qualitative study. Int. J. Qual. Stud. Health Well-Being 17, 2028348.